

Topology optimization for multi-axis machining

Langelaar, Matthijs

DOI

[10.1016/j.cma.2019.03.037](https://doi.org/10.1016/j.cma.2019.03.037)

Publication date

2019

Document Version

Final published version

Published in

Computer Methods in Applied Mechanics and Engineering

Citation (APA)

Langelaar, M. (2019). Topology optimization for multi-axis machining. *Computer Methods in Applied Mechanics and Engineering*, 351, 226-252. <https://doi.org/10.1016/j.cma.2019.03.037>

Important note

To cite this publication, please use the final published version (if applicable).
Please check the document version above.

Copyright

Other than for strictly personal use, it is not permitted to download, forward or distribute the text or part of it, without the consent of the author(s) and/or copyright holder(s), unless the work is under an open content license such as Creative Commons.

Takedown policy

Please contact us and provide details if you believe this document breaches copyrights.
We will remove access to the work immediately and investigate your claim.

Green Open Access added to TU Delft Institutional Repository

'You share, we take care!' – Taverne project

<https://www.openaccess.nl/en/you-share-we-take-care>

Otherwise as indicated in the copyright section: the publisher is the copyright holder of this work and the author uses the Dutch legislation to make this work public.

Topology optimization for multi-axis machining

Matthijs Langelaar

Delft University of Technology, Delft, The Netherlands

Received 10 July 2018; received in revised form 9 March 2019; accepted 17 March 2019

Available online 27 March 2019

Highlights

- Enforce multi-axis machining restrictions within a topology optimization process.
- Capable of considering a large set of tool orientations.
- Particular cutting tool shapes and maximum insertion lengths can be included.
- Adds little computational effort compared to part performance analysis.
- Application example shows capability to generate optimized, machinable 3D parts.

Abstract

This paper presents a topology optimization approach that incorporates restrictions of multi-axis machining processes. A filter is defined in a density-based topology optimization setting, that transforms an input design field into a geometry that can be manufactured through machining. The formulation is developed for 5-axis processes, but also covers other multi-axis milling configurations, e.g. 2.5D milling and 4-axis machining by including the appropriate machining directions. In addition to various tool orientations, also user-specified tool length and tool shape constraints can be incorporated in the filter. The approach is demonstrated on mechanical and thermal 2D and 3D numerical example problems. The proposed machining filter allows designers to systematically explore a considerably larger range of machinable freeform designs through topology optimization than previously possible.

© 2019 Elsevier B.V. All rights reserved.

Keywords: Design for Manufacturing; Multi-axis milling; 5-axis machining; 2.5D milling; Topology optimization; Subtractive manufacturing

1. Introduction

Design for manufacturing (DfM) is a well established paradigm in engineering design. Cost and/or performance advantages can be gained by including manufacturability considerations in the earliest stages of the design process [1]. This has motivated the present research to consider machining restrictions in topology optimization. Of all engineering optimization methods available to designers, topology optimization stands out by its ability to generate well-performing designs already at the conceptual design stage. The popular density-based approach solves a material distribution optimization problem to meet the criteria set by a designer [2]. Since its inception researchers have worked to develop techniques to consider manufacturability within topology optimization in a DfM fashion, to generate realistic and relevant results. A recent overview is given by Vatanabe et al. [3].

E-mail address: m.langelaar@tudelft.nl.

<https://doi.org/10.1016/j.cma.2019.03.037>

0045-7825/© 2019 Elsevier B.V. All rights reserved.

The focus of this paper is on multi-axis machining. This is a widely used subtractive manufacturing technology for the production of metal parts, where the relative position and orientation of cutting tools and workpiece can be manipulated in 4 or 5 degrees of freedom. Unnecessary material is removed until the desired freeform part geometry remains. These multi-axis processes allow considerably higher geometrical complexity than 3-axis/2.5D milling, where only translations between part and tool are possible [4]. Even higher design freedom is offered by metal additive processes, e.g. selective laser melting. However, in spite of the rapid developments in additive manufacturing, there is still a significant cost gap compared to machining [5]. Multi-axis machining may form an interesting option between these alternatives, depending on part size, series, material and available cutting speeds, and part geometry. DfM-based topology optimization approaches can help designers to make a rational cost/performance trade-off between the available manufacturing technologies.

Thus far, to our knowledge, no approach for multi-axis machining-based topology optimization has been reported. Here we briefly review related efforts for 2.5D machining and other manufacturing restrictions involving similar challenges. For a more general overview of research on the broader topic of manufacturing constraints for topology optimization, the reader is referred to recent surveys [3,6,7]. Regarding the topic of feature size control, we refer to [8] and the references therein.

Specifically for 2.5D machining, Liu et al. [9] have introduced a feature-based approach embedded in a level-set framework. Using geometrical feature fitting combined with shape optimization, a set of parameterized 2.5D features was optimized into a machinable geometry. In the density-based setting, Vatanabe et al. [3] proposed a unified projection-based approach to manufacturing constraints. The paper discusses 2.5D milling, but also turning, extrusion, casting and other processes. The formulation for milling is not discussed in detail, but a variable-mapping scheme is introduced that prevents undercuts or internal holes, which could serve to implement a 2.5D milling constraint.

Other related topology optimization studies concentrate on casting or draw direction constraints, which are similar to 2.5D machining in the sense that no undercuts are allowed from a specified single direction. In a density-based setting various authors have presented casting constraints. Approaches vary from introducing constraints between adjacent densities (e.g. [10,11], and even for > 2 directions in [12]), re-parameterizations and projections involving smoothed Heaviside functions (e.g. [3,13,14]), and the use of an auxiliary steady-state heat transfer problem involving unidirectionally conductive material to detect and suppress internal voids and undercuts [15]. An earlier evolutionary approach is described in [16]. Casting constraints for level-set-based formulations were presented in [17–19]. These approaches rely on projecting the boundary velocity vectors, in the parting direction of the mold. This modifies the way the boundary can evolve, and no undercuts can develop.

In contrast to all studies mentioned above, the aim of this paper is to propose an approach to optimize parts for multi-axis machining of 3D objects. In addition to the inclusion of a multitude of tool orientations, we also consider it important for practical relevance to address two additional aspects: the fact that the cutting tool has a particular size and shape, which needs to be accounted for, and the fact that its insertion length might be bounded. Instead of introducing many constraints in the optimization problem, the restriction is achieved by a new machining filter, that adds limited computational cost to the optimization process.

The remainder of this paper is organized as follows: after defining the problem setting in more detail, Section 2 describes the formulation of the proposed filter and its various components. Numerical 2D and 3D results are presented in Section 3, followed by a bracket application example. Subsequently, Section 4 provides additional discussion, after which Section 5 concludes this paper.

2. Formulation

2.1. Problem setting and approach

Before presenting the mathematical formulation of the proposed machining filter, this subsection first outlines the conceptual idea behind it. For clarity, the concepts are illustrated in 2D, but they apply to general multidirectional machining of 3D objects. The philosophy of the proposed method is to transform any given input density field into a machineable workpiece geometry. It can be viewed as a ‘machining filter’, that restricts the solution space to machineable designs only. In its most basic form, it involves a prismatic cutting tool and a single tool orientation. We consider tools that allow cutting of the workpiece both in sideways and axial directions, such as end mill cutters. Since any cutout that can be created by sideways cutting can also be created by axial insertion, but not

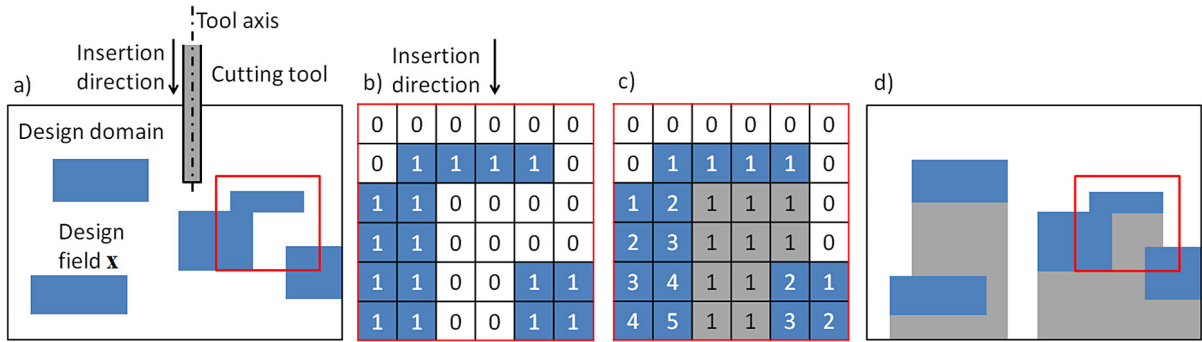


Fig. 1. (a) Prismatic tool definition. The blue regions represent an arbitrary density field \mathbf{x} . (b) Example input density field detail. (c) Obtained density field detail after cumulative summation of densities in insertion direction. (d) After cumulative summation of densities in the insertion direction, the inaccessible regions (gray) have nonzero density values. The resulting field defines a machineable geometry.

vice versa, we focus the machining filter on cutting operations where the insertion direction is aligned with the tool axis (Fig. 1(a)). A realizable design is a design where the cutting tool has unrestricted access to each point of its surface. The tool must at least be able to make an unobstructed axial approach to each surface point, as in plunge milling or drilling operations. This principle is equivalent to ‘posture reachability’ as defined in [20].

Starting point is a typical density-based topology optimization setting, where a regular finite element grid is used and the density of every element controlled by an associated design variable x_e . For simplicity, the tool axis and insertion direction is chosen parallel to a principal mesh direction. First the most precise tool is considered, with a width equal to element edge length h and with unrestricted length. This does not rule out use of larger tools to speed up final production, but for definition of the part in the conceptual design phase the finest tool is considered.

As recognized in other studies on topology optimization involving milling and casting constraints (e.g. [3,13]), machinability means that the density field must be monotonically increasing in the insertion direction. In this way, no internal holes can exist that are inaccessible for a cutting tool. Instead of introducing constraints or new parameterizations to enforce this, we simply construct this monotonically increasing field from the input density field by the cumulative summation of element densities in the tool insertion direction, as illustrated in Fig. 1(b,c). This is a linear operation of low computational complexity. The regions that can be cut remain at low density, while elsewhere in the domain density values can exceed one. By applying a final Heaviside projection step, a machineable physical density field is obtained (Fig. 1(d)).

This cumulative summation forms the basis of the proposed machining filter and allows the consideration of multiple tool orientations without increasing the number of design variables. Fig. 2 provides a flowchart of the machining filter process, starting with an input density field \mathbf{x} to which a density filter $\mathcal{F}(\mathbf{x})$ [21] is applied to impose a minimum length scale on the design. To handle multiple tool orientations conveniently, the summation direction is adjusted. To this end, m mappings are defined that transform the density field to a suitably rotated configuration $\mathbf{m}^{(i)}$, before application of the cumulative summation \mathcal{C} . Note that tool orientation is not treated as a continuous design variable, instead a finite set of m orientations is considered. The influence of different orientation sets is studied in Section 3. Restrictions such as the cutting tool length and shape are introduced as optional extensions, denoted in Fig. 2 by operators \mathcal{L} and \mathcal{E} , respectively. The accessible regions of all orientations are ultimately combined by first applying reverse mapping operations $\mathcal{R}^{(i)}$ to transform all fields back to the original reference orientation, followed by combining all accessible regions through application of intersection operation \mathcal{I} . To conclude, Heaviside projection \mathcal{H} renders a physical density field ρ of the machined workpiece. Full descriptions of each of the operations shown in Fig. 2 are provided in the remainder of this section. For readability, symbols of e.g. indices are occasionally redefined and reused between the subsections.

2.2. Multi-directional machining restriction

To conveniently implement the cumulative summation in any direction, an affine transformation is applied to density field $\tilde{\mathbf{x}}$ defined in reference coordinate system xyz , resulting in a mapped density field $\mathbf{m}^{(i)}$ in a new

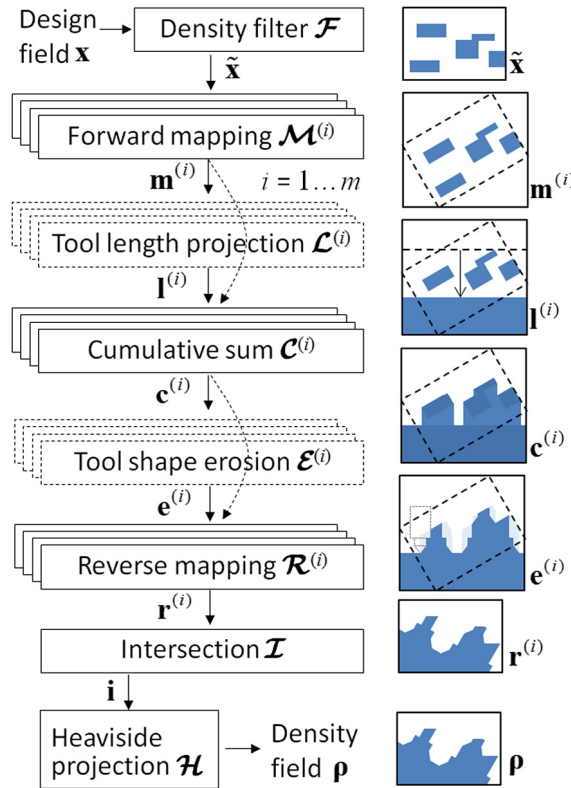


Fig. 2. Schematic representation of the proposed multi-axis machining filter, yielding $\rho(\mathbf{x})$. A (filtered) design field \mathbf{x} is mapped to various machining directions for processing by mappings $\mathcal{M}^{(i)}$. Dashed boxes represent optional operations (tool length and shape restrictions). Information from all machining directions is combined by an intersection operation \mathcal{I} in the reference domain, after reverse mapping $\mathcal{R}^{(i)}$. By a final Heaviside projection the physical density field ρ is generated.

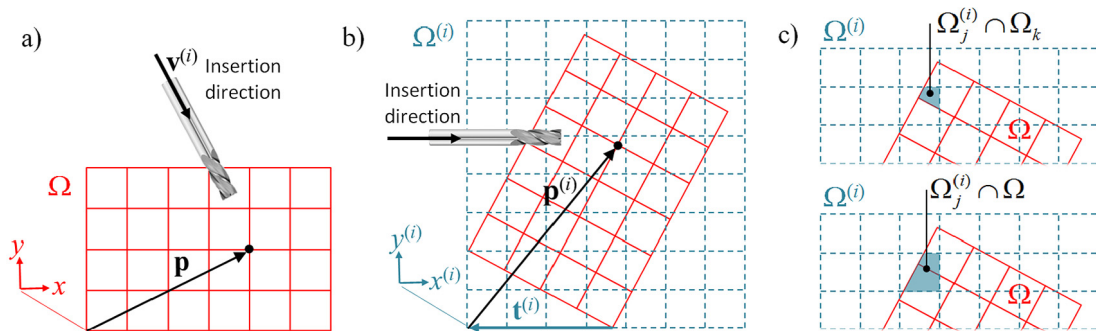


Fig. 3. 2D representation of the transformation applied to the reference domain Ω to an embedding box-shaped domain $\Omega^{(i)}$ (a,b), aligning the machining tool insertion direction with the $x^{(i)}$ -axis. The overlapping areas shown in (c) are used to define the associated mapping.

coordinate system $x^{(i)}y^{(i)}z^{(i)}$, see Fig. 3 for the 2D equivalent. We choose the transformation such that the $x^{(i)}$ -direction unit vector $\mathbf{e}_1^{(i)}$ corresponds to the tool orientation and insertion direction unit vector $\mathbf{v}^{(i)}$ defined in reference coordinates:

$$\mathbf{R}^{(i)} \mathbf{v}^{(i)} = \mathbf{e}_1^{(i)} \quad \Leftrightarrow \quad \mathbf{v}^{(i)} = \mathbf{R}^{(i)\text{T}} \mathbf{e}_1^{(i)} \tag{1}$$

with $\mathbf{R}^{(i)}$ a suitable rotation matrix. From this equation, the first row of $\mathbf{R}^{(i)}$ follows to be $\mathbf{v}^{(i)\text{T}}$. The second row is an arbitrary unit vector orthogonal to $\mathbf{v}^{(i)}$, and the third row is given by the cross product of the preceding two.

Density field $\tilde{\mathbf{x}}$ is defined on, or contained in, a box-shaped domain Ω of $n_x \times n_y \times n_z$ elements. After rotation, the dimensions of a new box-shaped embedding domain $\Omega^{(i)}$ are found by the transformed coordinates of the original corner points. A translation vector $\mathbf{t}^{(i)}$ is introduced to set the origin of the embedding domain at $\mathbf{0}$. The new domain is discretized with a mesh of equal element size, and its dimensions are increased to allow an integer number of elements in each principal direction. Each point \mathbf{p} in the reference domain can now be mapped to a corresponding point $\mathbf{p}^{(i)}$ in the new coordinate system:

$$\mathbf{p}^{(i)} = \mathbf{R}^{(i)\text{T}} \mathbf{p} + \mathbf{t}^{(i)}. \tag{2}$$

Given the point-to-point mapping defined by Eq. (2), density field $\tilde{\mathbf{x}}$ can be transformed to mapped density field $\mathbf{m}^{(i)}$ defined on the rotated domain $\Omega^{(i)}$. This operation is described by a linear mapping matrix $\mathbf{M}^{(i)}$, such that

$$\mathbf{m}^{(i)} = \mathbf{M}^{(i)} \tilde{\mathbf{x}}, \tag{3}$$

where the density fields are arranged as column vectors. Following the conventional density-based setting, densities on reference mesh Ω define a piecewise constant density field. The coefficients $M_{jk}^{(i)}$ of the sparse and generally nonsquare mapping matrix $\mathbf{M}^{(i)}$ are given by volume ratios [22]:

$$M_{jk}^{(i)} = \int_{\Omega_j^{(i)} \cap \Omega_k} dV \ / \ \int_{\Omega_j^{(i)} \cap \Omega} dV. \tag{4}$$

Here subscripts indicate the domain of individual mesh elements within the reference or embedding domain. The different integration domains are illustrated in Fig. 3(c). For elements in the embedding domain $\Omega^{(i)}$ that do not intersect the transformed reference domain, i.e. $\Omega_j^{(i)} \cap \Omega = 0$, by definition $M_{j*}^{(i)} \equiv 0$. The integrals in Eq. (4) are evaluated through numerical integration, and this initialization process is only needed once at the start of an optimization. To map the integration point locations between the domains, Eq. (2) is used. With this, the forward mapping operation \mathcal{M} in Fig. 1 has been fully defined, and consists of a sparse matrix–vector multiplication.

2.3. Cutting tool length

A next step in the milling filter chain shown in Fig. 2 is to account for a maximum cutting tool length, i.e. a maximum insertion depth. With the $x^{(i)}$ -direction being the insertion direction after the preceding mapping operation, a simplistic way to implement this is to set element densities to 1.0 from a certain $x^{(i)}$ -coordinate. However, this assumes the domain boundary as the reference plane to measure insertion depth, which is overly restrictive. Instead, the outermost part feature (i.e. with the lowest $x^{(i)}$ -coordinate) should be used as the reference plane. With respect to this, an end stop should be placed in the domain at the provided tool length/cutting depth L . In the considered discretized setting, L is expressed in an integer number of element lengths. A schematic overview of the proposed procedure is given in Fig. 4.

To cast this idea into a continuously differentiable procedure, first maximum densities are computed of element slabs that share the same $x^{(i)}$ -coordinate, indexed by p . A KS-function [23] is used as a smooth approximate maximum operator:

$$\hat{m}_{[p]}^{(i)} = \frac{1}{P_L} \ln \left(\frac{1}{n_{yz}^{(i)}} \sum_{q=1}^{n_y^{(i)}} \sum_{r=1}^{n_z^{(i)}} e^{P_L m_{[p,q,r]}^{(i)}} \right), \tag{5}$$

where $n_{yz}^{(i)} = n_y^{(i)} \cdot n_z^{(i)}$ is the number of elements in a slab orthogonal to the insertion direction, P_L is an aggregation factor and $[p, q, r]$ are Cartesian indices of entries of the density field $\mathbf{m}^{(i)}$. To prevent numerical overflow problems in combination with subsequent steps in the machining filter procedure, $\hat{\mathbf{m}}^{(i)}$ is transformed by a mapping function that bounds the highest values to 1:

$$\tilde{m}_{[p]}^{(i)} = \hat{m}_{[p]}^{(i)} e^{1 - \hat{m}_{[p]}^{(i)}}. \tag{6}$$

Finally, these bounded slab maxima are shifted by L and added to the input density field $\mathbf{m}^{(i)}$. This creates an end stop at the correct insertion depth, because empty slabs do not give a contribution. Thus, a new density field $\mathbf{l}^{(i)}$ is obtained by:

$$l_{[p,q,r]}^{(i)} = m_{[p,q,r]}^{(i)} + (p > L) \tilde{m}_{[p-L]}^{(i)}, \quad p = 1 \dots n_x^{(i)}, q = 1 \dots n_y^{(i)}, r = 1 \dots n_z^{(i)}. \tag{7}$$

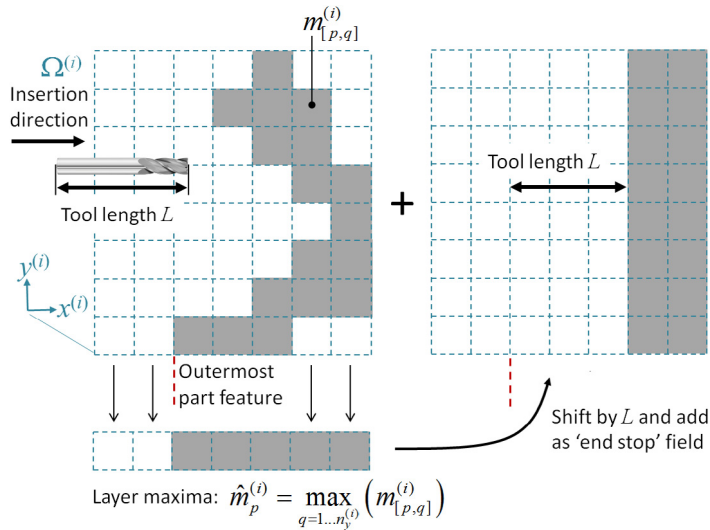


Fig. 4. 2D representation of the way a specified tool length L is accounted for. First the maximum density values are identified for layers orthogonal to the insertion direction, to detect the outermost feature of the design. Next, after shifting this data by L it is added to the density field to create an end stop.

This defines the operation $\mathbf{I} = \mathcal{L}(\mathbf{m})$ that accounts for tool length. Note that the first L slabs in the insertion direction are not altered. This is in agreement with the fact that any feature with a depth less than tool length L should not be affected by the tool length restriction. The operation \mathcal{L} involves a nonlinear KS maximum and bounding function. When not strictly necessary, it is an option to omit this operation from the machining filter.

2.4. Evaluating tool access by cumulative summation

As already outlined in Section 2.1 and illustrated in Fig. 1(b,c), the density field is transformed into a machineable density field through cumulative summation. This step forms the heart of the proposed machining filter, and is denoted by operation $\mathcal{C}^{(i)}$ in Fig. 2. The input density field can be either $\mathbf{I}^{(i)}$ or $\mathbf{m}^{(i)}$, depending on whether a tool length restriction is considered. In the formulation given here input field $\mathbf{m}^{(i)}$ is assumed. The output density field $\mathbf{c}^{(i)}$ is created by cumulative summation in the insertion direction ($x^{(i)}$ -direction):

$$\begin{cases} c_{[1,q,r]}^{(i)} = m_{[1,q,r]}^{(i)}, & q = 1 \dots n_y^{(i)}, r = 1 \dots n_z^{(i)}, \\ c_{[p,q,r]}^{(i)} = c_{[p-1,q,r]}^{(i)} + m_{[p,q,r]}^{(i)}, & p = 2 \dots n_x^{(i)}, q = 1 \dots n_y^{(i)}, r = 1 \dots n_z^{(i)}. \end{cases} \quad (8)$$

This is a linear operation, and can therefore also be written as:

$$\mathbf{c}^{(i)} = \mathbf{C}^{(i)} \mathbf{m}^{(i)} \quad (9)$$

with $\mathbf{C}^{(i)}$ a suitably constructed sparse matrix reflecting Eq. (8), and the density fields in vector form. Note that the resulting field $\mathbf{c}^{(i)}$ can contain values larger than one. This is not a problem for the remaining operations, and in the final step the field will be transformed to physical density values in the $[0, 1]$ -range through Heaviside projection.

2.5. Cutting tool shape

A next optional step is to account for a particular tool shape. Consistent with typical machining operations involving fast spinning cutting tools, we consider tools to be in effect axisymmetric, characterized by a single diameter or multiple diameters and segment lengths in case of a stepped tool geometry. Instead of the actual tool geometry, the geometry of the hole created in the workpiece when the tool is inserted axially is considered relevant for design. This is the effective tool envelope (Fig. 6(a)), which is taken as the tool shape in the following. In

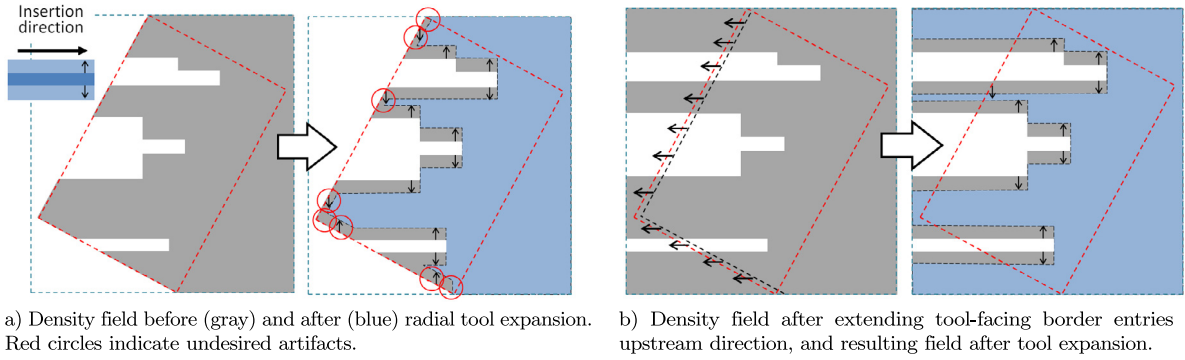


Fig. 5. 2D illustration indicating the need to expand tool-facing border densities of the mapped reference domain in the direction from which the tool is inserted.

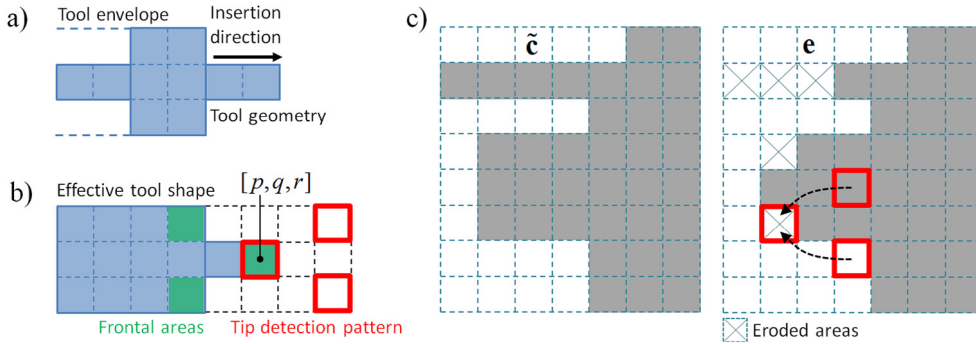


Fig. 6. 2D representation of the way a certain tool shape is accounted for. (a) Definition of tool envelope. (b) Definition of frontal areas and tooltip detection pattern used in the erode operation. (c) Illustration of the effect of the toolshape-based erode operation on density field $\tilde{\mathbf{c}}$. For one eroded density the dependence on other members of the pattern is indicated by arrows.

the discretized design domain, the tool shape is assumed to be defined in terms of integer element units, and a corresponding radial expansion of the holes defined in the preceding steps will be performed.

Imposing the cutting tool shape on the workpiece is performed in two steps. First, it is necessary to expand the densities on the border of the mapped reference domain facing the tool tip in the direction from which the tool is inserted, i.e. upstream. As illustrated in Fig. 5(a), without this expansion step void regions of the embedding domain may cut into the workpiece by radial tool expansion. This would result in uncontrollable cutting of the boundary regions of the part, since the optimizer cannot control the densities in the embedding domain outside the mapped reference domain. By expanding the border densities into the embedding domain, this undesired effect is prevented, as illustrated in Fig. 5(b). The expansion step is defined as:

$$\begin{cases} \tilde{c}_{[p,q,r]}^{(i)} = c_{[\hat{p},q,r]}^{(i)} & 1 \leq p < \hat{p}, \\ \tilde{c}_{[p,q,r]}^{(i)} = c_{[p,q,r]}^{(i)} & \text{otherwise.} \end{cases} \quad (10)$$

Here \hat{p} is the index of the first density belonging to the mapped reference domain, in tool insertion direction $x^{(i)}$. This linear expansion operation can be written as $\tilde{\mathbf{c}}^{(i)} = \mathbf{E}^{(i)} \mathbf{c}^{(i)}$, with sparse linear operator $\mathbf{E}^{(i)}$. This forms the first step of the process to account for the cutting tool shape.

The second step performs the radial tool expansion. The void regions present in the expanded input density field $\tilde{\mathbf{c}}$ must be realized by machining. Features that may block tool access into these regions should be removed. One way to approach this operation, is to consider each void element as a tool tip position and project the tool shape as a void region to other parts of the domain. This involves a large amount of design variables. A leaner way to effectively define the same operation, is to only project the frontal areas of the tool as void regions (see Fig. 6(b)). This is possible because after the cumulative summation (Section 2.4), the density field is monotonically increasing

in the insertion direction. When the element at the tool tip position is void, the other frontal elements need to be void as well to ensure tool access. By sweeping through the mesh, this leaner operation will still cover the full tool shape.

To implement this concept, a suitable approach is to use a smooth minimum. This operation can be used to set an element density to void when one or several element densities of a considered set or pattern are void. The classical erode filter [24] does this for a set of densities located within a certain distance of an element, but the same principle can be applied to other patterns. In the present case, the controlling element is the tool tip. The relevant set is therefore found by considering all potential tool tip positions for which a given element is one of the frontal elements. This results in a pattern that corresponds to the frontal areas of the tool, mirrored in the plane normal to the tool axis (Fig. 6(b)). Using this ‘tip detection’ pattern combined with a KS-based smooth minimum, in a ‘patterned erosion’ operation the tool shape can be applied to the workpiece. All regions that are void in the density field $\tilde{\mathbf{c}}$ will remain void, while additional void regions are created where needed to ensure tool access, as illustrated in Fig. 6(c). This operation is given by:

$$e_{[p,q,r]}^{(i)} = \frac{1}{P_E} \ln \left(\frac{1}{n_E} \sum_{s=1}^{n_E} e^{P_E \tilde{\mathbf{c}}_{[p+dp_s, q+dq_s, r+dr_s]}^{(i)}} \right), \quad p = 1 \dots n_x^{(i)}, q = 1 \dots n_y^{(i)}, r = 1 \dots n_z^{(i)}, \quad (11)$$

where n_E is the number of elements in the tool tip detection pattern, defined by relative element offsets $d\mathbf{p}$, $d\mathbf{q}$ and $d\mathbf{r}$, with the tool tip having offset 0. $P_E < 0$ is the KS aggregation parameter. This operation is applied to all elements in the domain in order to ensure full tool access, with adequate offset selection or ghost layers to handle boundary regions. The complete tool shape operation consisting of the expansion and erosion step is denoted \mathcal{E} and produces output field \mathbf{e} . As with the tool length operator, it is nonlinear due to the KS minimum. When enforcing a tool shape is not strictly needed, it is an option to omit this step from the machining filter.

2.6. Physical workpiece extraction

To complete the machining filter, the density fields obtained for multiple tool orientations must be combined into a single field, and subsequently density values must be restricted to a physical range. These operations are performed in three steps (Fig. 2):

1. Reverse mapping of density fields $\mathbf{c}^{(i)}$ to the reference mesh. This operation is analogous to the forward mapping, but with the roles of the source and target meshes reversed. For the formulation we refer to Section 2.2. This results in $\mathbf{r}^{(i)} = \mathcal{R}^{(i)}(\mathbf{c}^{(i)}) = \mathbf{R}^{(i)}\mathbf{c}^{(i)}$, i.e. a linear operation involving sparse mapping matrix $\mathbf{R}^{(i)}$. Note that in this definition input fields $\mathbf{c}^{(i)}$ are assumed. In case the optional tool shape erosion procedure is applied, $\mathbf{e}^{(i)}$ is used instead.
2. Intersection of all density fields on the reference mesh. Each density field contains void regions cut by the tool in a specific orientation. By taking the intersection, all cut regions are combined into those of the actual machined workpiece: $\mathbf{i} = \mathbf{r}^{(1)} \cap \mathbf{r}^{(2)} \cap \dots \cap \mathbf{r}^{(m)} = \mathcal{I}(\mathbf{r}^{(1)}, \dots, \mathbf{r}^{(m)})$. A differentiable intersection operation can be implemented by taking the elementwise smooth minimum over all fields. For this, again a KS-function is used:

$$i_j = \frac{1}{P_I} \ln \left(\frac{1}{m} \sum_{i=1}^m e^{P_I r_j^{(i)}} \right), \quad (12)$$

with m the number of tool orientations, j a certain element index in the reference domain, and $P_I < 0$ as the KS aggregation parameter.

3. Heaviside projection to map entries of \mathbf{i} into the physical density range $[0, 1]$, yielding the final density field $\rho = \mathcal{H}(\mathbf{i})$. For this step the well known smooth Heaviside function is used [25]:

$$\rho_j = \frac{\tanh(\beta\eta) + \tanh(\beta(i_j - \eta))}{\tanh(\beta\eta) + \tanh(\beta(1 - \eta))}, \quad (13)$$

with β controlling the steepness of the smooth Heaviside. In this paper we fix the parameter η to 0.5.

This final procedure concludes the machining filter definition. Note that in its basic form, without the optional tool length and tool shape operations, all steps up to the intersection \mathcal{I} are linear operations, and can be represented by a single linear operator $\mathbf{FM}^{(i)}\mathbf{C}^{(i)}\mathbf{R}^{(i)}$. Both tool geometry operations and the final intersection involve KS functions over subsets of element densities, and the concluding Heaviside projection also is nonlinear.

2.7. Sensitivity analysis

Given a response $f(\boldsymbol{\rho})$ and its sensitivity with respect to the physical densities $\partial f/\partial \boldsymbol{\rho}$, it follows from the definition of the full machining filter that:

$$\frac{\partial f}{\partial x_j} = \frac{\partial f}{\partial \rho_\alpha} \frac{\partial \rho_\alpha}{\partial x_j} = \frac{\partial f}{\partial \rho_\alpha} \frac{\partial \rho_\alpha}{\partial i_\beta} \left(\sum_{i=1}^m \frac{\partial i_\beta}{\partial r_\gamma^{(i)}} \frac{\partial r_\gamma^{(i)}}{\partial \tilde{x}_\theta} \right) \frac{\partial \tilde{x}_\theta}{\partial x_j}, \quad \text{with} \quad \frac{\partial r_\gamma^{(i)}}{\partial \tilde{x}_\theta} = \frac{\partial r_\gamma^{(i)}}{\partial e_\delta^{(i)}} \frac{\partial e_\delta^{(i)}}{\partial c_\epsilon^{(i)}} \frac{\partial c_\epsilon^{(i)}}{\partial l_\zeta^{(i)}} \frac{\partial l_\zeta^{(i)}}{\partial m_\eta^{(i)}} \frac{\partial m_\eta^{(i)}}{\partial \tilde{x}_\theta} \quad (14)$$

where Einstein summation applies to all repeated subscripts. Instead of forming all Jacobians in Eq. (14) and multiplying them to create the full Jacobian $d\boldsymbol{\rho}/d\mathbf{x}$, it is more efficient to transform the provided sensitivity $\partial f/\partial \rho_\alpha$ step by step through all the operations, from left to right. This only requires matrix–vector multiplications instead of matrix–matrix multiplications. This transformation of the sensitivity follows the reversed order through the machining filter steps. The Jacobians of the density filter, both mappings, the cumulative summation and the axial tool shape expansion step are given directly by the involved sparse linear operators, i.e.

$$\frac{d\tilde{\mathbf{x}}}{d\mathbf{x}} = \mathbf{F}, \quad \frac{d\mathbf{m}^{(i)}}{d\tilde{\mathbf{x}}} = \mathbf{M}^{(i)}, \quad \frac{d\mathbf{r}^{(i)}}{d\mathbf{e}^{(i)}} = \mathbf{R}^{(i)}, \quad \frac{d\mathbf{c}^{(i)}}{d\mathbf{m}^{(i)}} = \mathbf{C}^{(i)}, \quad \frac{d\tilde{\mathbf{c}}}{d\mathbf{c}} = \mathbf{E}. \quad (15)$$

The final Heaviside projection \mathcal{H} is an elementwise operation, thus its Jacobian is a diagonal matrix with the following entries:

$$\frac{\partial \rho_\alpha}{\partial i_\alpha} = \frac{\beta (1 - \tanh^2(\beta(i_\alpha - \eta)))}{\tanh(\beta\eta) + \tanh(\beta(1 - \eta))}. \quad (16)$$

This leaves the Jacobians of the nonlinear intersection, tool shape erosion and tool length operations. These are all defined using KS aggregation functions, with different inputs: the intersection combines elementwise values from different tool orientation fields, the tool shape erosion involves entries within the tool tip detection pattern, and the tool length operation combines densities of entire slabs orthogonal to the insertion direction. To cover all these operations, Eq. (17) introduces a generic KS function for a general input set:

$$t_i = KS(\mathbf{s}) = \frac{1}{P} \ln \left(\frac{1}{|S_i|} \sum_{s_k \in S_i} e^{P s_k} \right), \quad (17)$$

where $|S_i|$ denotes the number of entries of the index set S_i . The corresponding Jacobian terms are:

$$\frac{\partial t_i}{\partial s_j} = \frac{e^{P s_j}}{\sum_{s_k \in S_i} e^{P s_k}}. \quad (18)$$

From this, the Jacobians $\partial \mathbf{i}/\partial \mathbf{r}^{(i)}$, $\partial \mathbf{e}^{(i)}/\partial \hat{\mathbf{c}}^{(i)}$ and $\partial \hat{\mathbf{m}}^{(i)}/\partial \mathbf{m}^{(i)}$ follow directly by applying the respective index sets S_i and aggregation parameter P . The obtained smooth maxima in the tool length operation \mathcal{L} are subsequently transformed by Eq. (6) and added to all elements in layers shifted in the insertion direction (Eq. (7)). Consequently, the sensitivities become:

$$\frac{\partial l_{[p,q,r]}^{(i)}}{\partial m_{[s,t,u]}^{(i)}} = \delta_{ps} \delta_{qr} \delta_{ru} + (p \leq n_x^{(i)} - L) \frac{\partial \tilde{m}_{[p+L]}^{(i)}}{\partial m_{[s,t,u]}^{(i)}} \quad \text{with} \quad \frac{\partial \tilde{m}_{[p]}^{(i)}}{\partial \mathbf{m}^{(i)}} = \left(1 - \hat{m}_{[p]}^{(i)} \right) e^{1 - \hat{m}_{[p]}^{(i)}} \frac{\partial \hat{m}_{[p]}^{(i)}}{\partial \mathbf{m}^{(i)}}, \quad (19)$$

where the term $(p \leq n_x^{(i)} - L)$ indicates that the following derivative is only present for layers from which information was shifted downstream. Finally, KS aggregation can be prone to numerical overflow. This is avoided by transforming all inputs of KS functions to $\hat{s} = \ln(s)$ when $s > 1$, and accounting for the corresponding derivatives $d\hat{s}/ds = 1/s$.

3. Numerical results

3.1. Test problems and settings

As the focus of this paper is on the proposed multidirectional machining filter, well-known mechanical and thermal compliance minimization problems are used as test problems. For additional detail on these problems,

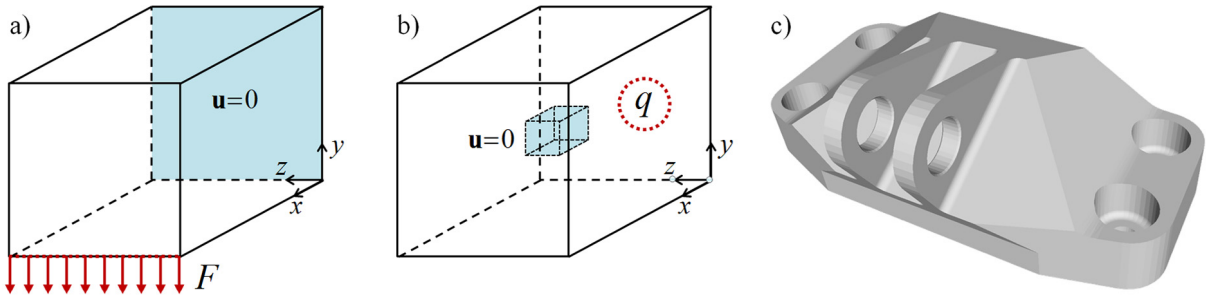


Fig. 7. (a) Mechanical cantilever beam problem, clamped at the $x = 0$ -plane with a distributed line load with resultant F of total unit magnitude applied at the free end. (b) Thermal block problem, with zero temperature boundary condition on a centered box 10 times smaller than the domain, subjected to a body heat load q of total unit magnitude. (c) GE engine bracket design domain [27], 3D only. For 2D versions of (a,b), all loads and boundary conditions are projected on the x, y -plane.

reference is made to [2]. Both optimization problems can be stated as:

$$\begin{aligned}
 \min_{\mathbf{x}} \quad & C = \mathbf{f}^T \mathbf{u}(\boldsymbol{\rho}) \\
 \text{s.t.} \quad & V(\boldsymbol{\rho})/V_{\max} - 1 \leq 0, \\
 & \mathbf{K}(\boldsymbol{\rho})\mathbf{u}(\boldsymbol{\rho}) = \mathbf{f}, \\
 & 0 \leq \mathbf{x} \leq 1.
 \end{aligned} \tag{20}$$

Here \mathbf{K} , \mathbf{u} and \mathbf{f} denote the finite element system stiffness (or conductivity) matrix, displacement (or temperature) vector and mechanical (thermal) load vector, respectively. The Young's modulus and conductivity of solid material are set to unity. V and V_{\max} are the actual and allowed volume of the machined part relative to the design domain. Density field $\boldsymbol{\rho}$ is constructed by application of the machining filter introduced in Section 2 to design variable field \mathbf{x} . SIMP material interpolation (see e.g. [2]) is applied to the physical densities with penalization exponent p , while maintaining lower bounds E_{\min} and C_{\min} on the respective material properties at $\rho = 0$. The sensitivity of the objective with respect to the physical density field $\boldsymbol{\rho}$ is given by:

$$\frac{\partial C}{\partial \rho_i} = -\mathbf{u}^T \frac{\partial \mathbf{K}}{\partial \rho_i} \mathbf{u}. \tag{21}$$

This sensitivity is subsequently transformed to $\partial C/\partial x_i$ following the procedure described in Section 2.7.

The following subsections present 2D and 3D results for both problems. The 2D setting is better suited to verify particular aspects of the machining filter, while the 3D setting allows the demonstration of the effectiveness of the approach in a practical application setting, and for the consideration of problems inspired on actual 5-axis milling. In both the 2D and 3D test cases similar load scenarios and boundary conditions are considered: the mechanical problem involves a typical cantilever beam design case (Fig. 7(a)), and for the thermal problem the domain is subjected to a incoming body heat flux, with a fixed-temperature heat sink defined at the center (Fig. 7(b)). This problem tends to form branching structures that fill the available domain,¹ where the effect of tool shape and orientation is clearly recognizable. A 3D application case is presented in Section 3.4, inspired on the GE engine bracket design problem (Fig. 7(c)).

All optimizations are performed using the MMA algorithm [28], with default settings except for the ASY_INIT parameter, which has been reduced from 0.5 to 0.1. This limits design changes at the start, which is helpful in view of the nonlinearity added by the filter. MMA is sensitive to scaling, therefore in the first iteration a normalization constant is determined to set the initial objective to 10.0. When the objective value drops below 0.1 during the optimization process, the normalization constant is decreased by a factor 10. For simplicity, all design variables are set to relative volume fraction V_{\max} initially. This results in fully solid initial physical densities nearly everywhere, similar to the blank before machining. The optimization process is terminated when the relative change in objective value in subsequent feasible iterations drops below 10^{-4} , with a maximum of 100 iterations. The machining filter is

¹ Note that remarkably, Yan et al. [26] have recently proven that the typical branching structures found for this problem are in fact local optima, and optimal designs feature lamellar or needle-like structures instead.

Table 1

Problem parameter values used in the numerical experiments.

Parameter	Mechanical			Thermal	
	2D beam	3D beam	3D bracket	2D block	3D block
E_{\min} or C_{\min}	10^{-9}	10^{-9}	10^{-9}	10^{-3}	10^{-3}
ν	0.3	0.3	0.3	–	–
Domain ($n_x \times n_y \times n_z$)	$200 \times 100 \times 1$	$100 \times 50 \times 50$	$180 \times 110 \times 64$	$200 \times 200 \times 1$	$100 \times 100 \times 100$
Volume fraction V_{\max}	0.5	0.3	0.12	0.5	0.3
Density filter radius r_{\min}	3.0	1.5	1.5	3.0	1.5
KS-parameter P_L	8.0 or 12.0	8.0	8.0	8.0 or 16.0	12.0
KS-parameter P_E	–8.0 or –12.0	–8.0	–8.0	–8.0 or –16.0	–12.0
KS-parameter P_I	–8.0 or –12.0	–8.0	–8.0	–8.0 or –16.0	–12.0
SIMP penalization p	3.0 or 5.0	4.0	4.0	8.0 or 16.0	10.0
Heaviside β	4.0 or 8.0	4.0	4.0	8.0	6.0

Table 2Normalized compliances (C/C_{ref}) and iteration data of all test cases, with figure references. The top row cases are the unrestricted reference designs, except for Fig. 25 results (3D Mechanical), for which case 25(a) is the reference.

2D Mechanical			2D Thermal			3D Mechanical			3D Thermal		
Fig.	C/C_{ref}	It.	Fig.	C/C_{ref}	It.	Fig.	C/C_{ref}	It.	Fig.	C/C_{ref}	It.
8(a)	1.0	48	9(a)	1.0	100	16(a)	1.0	100	17(a)	1.0	92
8(b)	2.4	63	9(b)	1.4	75	16(b)	1.05	51	17(b)	6.4	100
8(c)	3.0	67	9(c)	1.5	100	16(c)	1.12	82	17(c)	9.4	100
8(d)	1.1	43	9(d)	1.6	83	19(a)	1.02	65	21(a)	1.2	42
8(e)	3.8	100	12(a)	1.2	100	19(b)	1.05	100	21(b)	1.2	95
8(f)	2.8	50	12(b)	1.3	100	19(c)	1.06	100	21(c)	1.5	44
11(a)	3.1	86	12(c)	1.1	84	20(a)	1.06	76	22(a)	1.6	86
11(b)	1.2	100	12(d)	1.1	80	20(b)	1.05	82	22(b)	1.9	87
11(c)	1.5	78	14(a)	1.5	87	20(c)	1.06	80	22(c)	1.8	99
13(d)	1.6	95	14(b)	1.5	100	23(a)	1.18	97	24(a)	2.0	100
13(e)	1.6	88	14(c)	1.6	100	23(b)	1.22	100	24(b)	2.9	59
13(f)	1.7	52	14(d)	1.9	90	25(a)	1.0	100			
13(g)	1.5	100	14(e)	4.5	66	25(b)	0.97	100			
13(h)	1.6	98	14(f)	9.7	57	25(c)	1.21	100			
13(i)	1.5	97				25(d)	1.32	100			

evaluated on the designs it generates within these limits. Nominal settings for various problem parameters listed in Table 1 are used, unless mentioned otherwise. The finite element modeling involved standard isoparametric 4-node quadrilateral elements with bilinear shape functions in 2D, and 8-node hexahedral elements with trilinear shape functions in 3D. All elements have edge length $h = 1.0$. In the 2D mechanical case, a plane stress setting is used.

3.2. Machining-based topology optimization tests: 2D

The following subsections report 2D test results that illustrate various aspects of the proposed machining filter. To demonstrate the different components of the filter separately, initially no tool length or shape restriction is applied, i.e. features can be cut as small as the mesh resolution allows (element size h). From Section 3.2.3 onward, dimensions of cutting tools are also considered. Presented results show the physical densities ρ as obtained, no post-processing has been applied. Only the most pertinent numerical findings are discussed here, the complete iteration and objective data for all cases is listed in Table 2.

3.2.1. Single tool orientation

This first set of tests involves mappings \mathcal{M} and \mathcal{R} , as well as the cumulative summation \mathcal{C} . Fig. 8 shows the reference design for the cantilever case (a), together with 5 single-orientation results. Schematic indicators in blue show the considered tool orientations. The 0° orientation denotes an insertion direction in the negative x -axis,

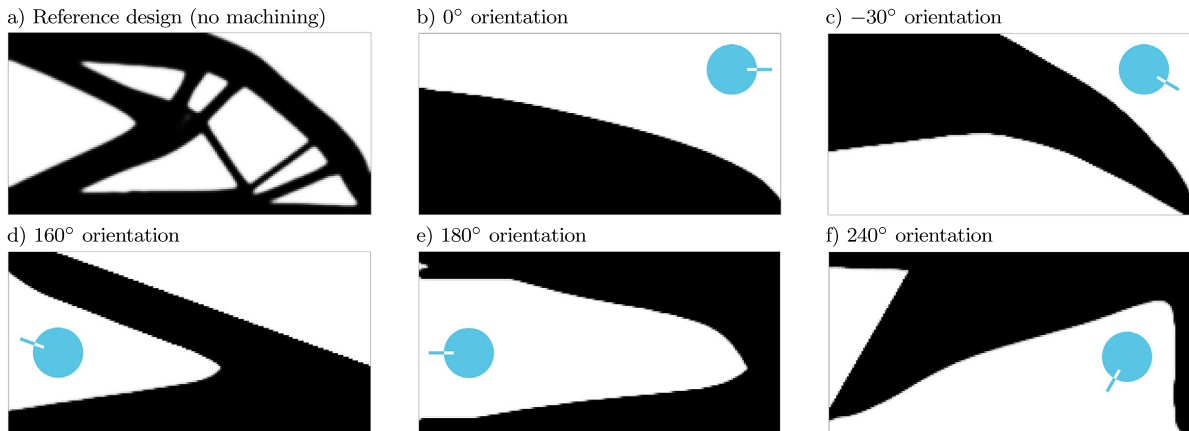


Fig. 8. Mechanical case, reference design (a) and designs obtained using various single tool orientations.

i.e. from the right. Other orientations follow by counterclockwise rotation. Cases took between approximately 40 and 70 iterations, except the 180°-case which used all allowed iterations. The reference solution is not manufacturable when considering only machining operations in the x, y -plane, and certainly not when only using a single tool orientation. The results clearly show that the unidirectional machining restriction strongly limits design freedom, which also has an impact on the structural performance. The 160°-case (Fig. 8(d)) falls within 10% of the reference design performance, but the other designs are considerably more compliant, by factors ranging from 2.4 to 3.8× (Table 2). The obtained designs also clearly illustrate that the machining filter is effective in enforcing the intended restriction for any chosen direction.

Results for the single-orientation thermal problem are shown in Fig. 9(b,c,d), together with the unrestricted reference solution (a). Also here the reference design is not manufacturable, as large parts of the structural boundary cannot be accessed from outside by a straight cutting tool. The designs obtained with machining filter exhibit distributed structures of conductive material that conduct the incoming heat from the entire domain to the central heat sink, within the limits of manufacturability. Performance is 40 to 60% worse compared to the reference design. Relatively strong penalization must be applied for this problem, otherwise the optimization process will yield compromise solutions using intermediate densities. The machining filter is not a means to suppress gray designs, and in Fig. 9(c) this is illustrated by a thin line of gray in the left upper corner. This design was obtained after the full 100 iterations, it is possible that the gray feature would have disappeared upon additional iterations. Note also that the 45°-case (Fig. 9(d)) is symmetric in domain, loading and boundary conditions, but the optimized result is not symmetric. This is likely caused by small round-off errors, that can break the symmetry of the process at some point of the optimization. When there is no clear performance benefit of a symmetric design over an asymmetric one, the design can develop asymmetric features. If a symmetric design is desired, it can always be enforced by e.g. a different design parametrization.

Fig. 10 shows several intermediate fields of the design depicted in Fig. 9(d). The input field $\tilde{\mathbf{x}}$ is rotated to the relevant orientation, producing mapped field \mathbf{m} . Note that the domain has expanded by this operation. Subsequent cumulative summation produces \mathbf{c} , which contains values approaching 90 in this case. Because of the wide range of values, the structural boundary (near value 1) is more difficult to distinguish visually. Mapping this field back to the original orientation yields \mathbf{r} , and after Heaviside projection Fig. 9(d) is obtained.

3.2.2. Multiple tool orientations

In the following test problems different tool orientations are combined, which also involves intersection \mathcal{I} . Fig. 11(a,b,c) show mechanical designs obtained for 2, 3 and 4 orientations. Case (a) combines 0 and -90° directions, which gives an increased design freedom over the 0°-case considered in Fig. 8(b). Still, the performance with multiple directions is worse than the single-direction case (3.1 vs. 2.4× the reference compliance, respectively), which indicates that an inferior local optimum has been found. Improvements are reached when adding a third direction of 180° (case (b)), to a compliance of only 20% beyond the reference. In Fig. 11(c) the restriction imposed

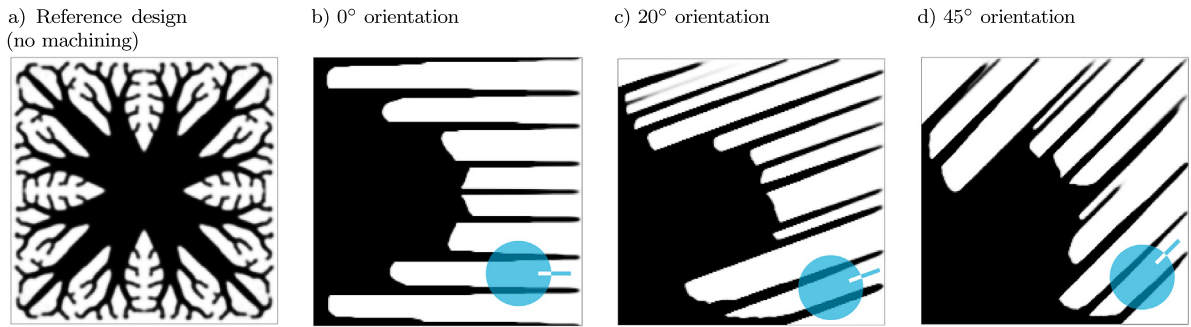


Fig. 9. Thermal case, reference design (a) and designs obtained using various single tool orientations.

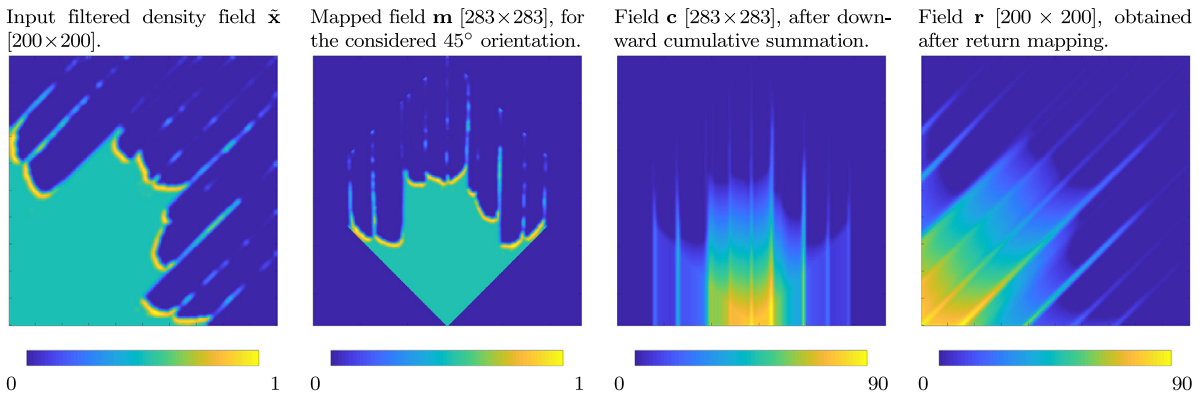


Fig. 10. Intermediate fields of the design shown in Fig. 9(d), where a single 45° orientation was considered.

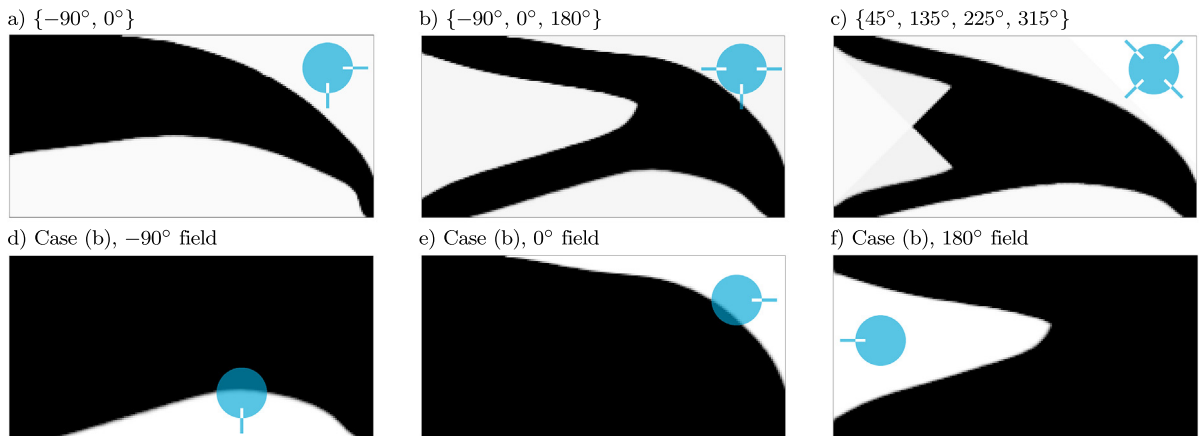


Fig. 11. Mechanical case, (a,b,c): designs obtained using multiple tool orientations. (d,e,f): Subfields $r^{(i)}$ for the 3 orientations considered in case (b), after Heaviside projection. Their intersection yields design (b).

by the selected directions can be recognized by the triangular shape on the left. The central region cannot be machined without removing material at the supports, which results in this compromise. In Fig. 11(d,e,f) the three single-orientation density fields $r^{(i)}$ from Fig. 11(b) are depicted. Their intersection forms the final design.

In the thermal case the orientations are more readily visible in the final designs, as the problem promotes structures to fill the domain as much as possible. Fig. 12 shows designs obtained for 2, 4, 12 and 37 directions. Note again that, certainly in fine-scale structures, symmetry is not preserved. Design (b) shows various disconnected

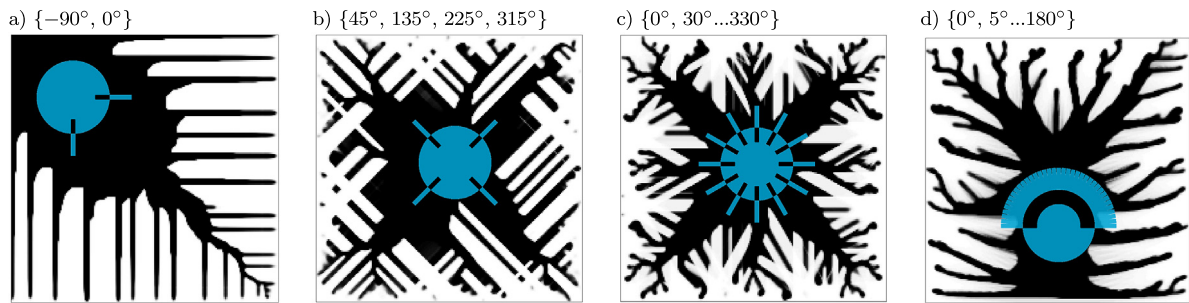


Fig. 12. Thermal case, designs obtained using multiple tool orientations.

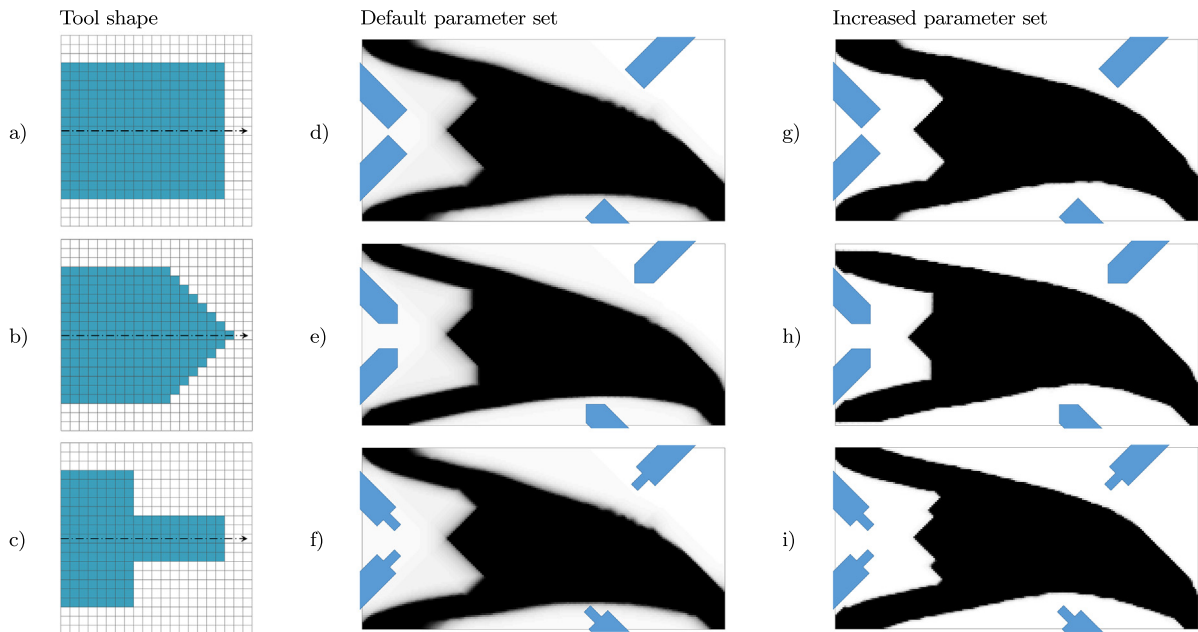


Fig. 13. Mechanical designs obtained using flat, conic and stepped tool tips, with tool orientations $\{45^\circ, 135^\circ, 225^\circ, 315^\circ\}$, similar to Fig. 11(c). All tools have a diameter of 15 elements.

pieces, caused by crossing toolpaths. In this thermal problem, disconnected conductive regions can be realized as the white regions are considered to consist of a substrate with low conductivity. In optimized designs, however, usually connected structures are observed. The machining restriction in this case forces the optimization process towards a different solution, and does not inherently disallow disconnected regions. All multi-direction cases improve in performance compared to their single-orientation counterparts, with cases (c) and (d) even achieving objective values within 10% of the reference (Fig. 9(a)), using less than the allowed 100 iterations. Thus combining many tool orientations through intersection proves effective.

3.2.3. Accounting for tool shape and length

Finally, we include tool shape (operator \mathcal{E}) and tool length (operator \mathcal{L}). Cutting tools with flat, conic and stepped tips are considered as shown in Fig. 13(a,b,c). All tools are $15h$ wide. For the mechanical tests, the 4-orientation case of Fig. 11(c) is used since it most clearly shows the tool outline. The designs in Fig. 13(d,e,f) were generated using the same parameter set as in the preceding cases without tool shape. Although the designs can be easily interpreted, there is a zone of intermediate density present at the structural boundary. The tool shape is imposed on the density field using KS-based erosion (Eq. (11)), and the crispness of the result depends on the applied KS-parameter P_E . When crisper designs are desired, this can be achieved by increasing parameters that

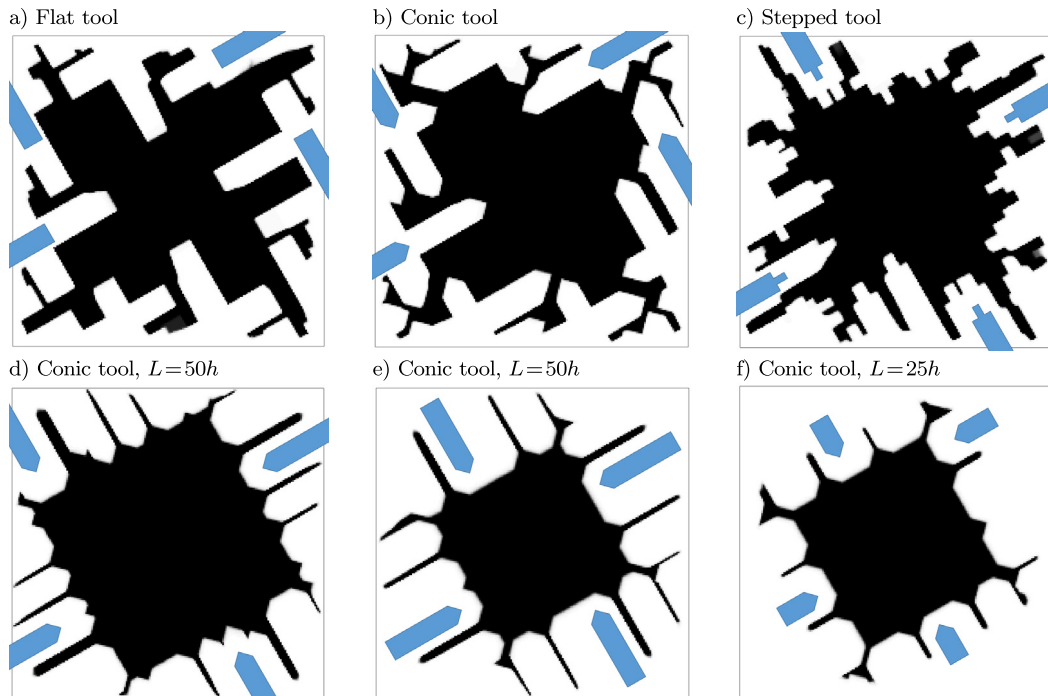


Fig. 14. Thermal case, designs obtained using various tool shapes, with tool orientations $\{30^\circ, 120^\circ, 210^\circ, 300^\circ\}$. All tools have a diameter of 15 elements. (a,b,c,d): default parameters. (e,f): reduced volume fraction (30%).

promote black–white designs: the KS aggregation parameters, but also the SIMP penalization exponent p and the Heaviside steepness parameter β . Using an increased parameter set (see Table 1, 2D mechanical) the designs shown in Fig. 13(g,h,i) were obtained. In general it is recommended to raise parameters when stacking more nonlinear aggregation operations and when increasing the number of aggregated quantities (tool shape definition entries, orientations). However, raising parameters values likely makes convergence harder as it increases the nonlinearity the filter adds to the problem, and should therefore be applied in moderation. In this case, all designs with the default parameter set converged faster than those using the increased parameters. Consistent with the fact that the region affected by the tool shape variations is relatively small, the performance of the obtained designs is comparable or slightly inferior to the case in Fig. 11(c) which used the highest cutting tool resolution (no tool shape). Being able to produce crisper density distributions, the designs with higher parameter values (Fig. 13(g,h,i)) are less affected by SIMP penalization and perform slightly better than their counterparts using the default parameter set.

The same three tool shapes are also employed in the thermal case, and Fig. 14(a,b,c) shows the obtained results. Also here, the increased parameter values listed in Table 1(2D thermal) are used. These parameters are higher than in the mechanical case, to counteract the tendency of this thermal problem to form compromise solutions consisting of intermediate densities, which the optimizer may favor over the coarser features enforced by the tool shape constraint. The tool shapes are clearly recognizable in the obtained designs, confirming again that arbitrary tool shapes are effectively introduced.

Finally, the conic tool shape is combined with a finite tool length, resulting in the designs in Fig. 14(d,e,f). The tool length is varied from 50 to 25 element lengths h , and also two different volume fractions are considered. Optimizations converged in approximately 90, 70 and 60 iterations. The resulting designs indeed show the intended feature that tool length leads to a maximum insertion length measured from the outermost part feature present in the considered tool insertion direction, instead of measuring from the design domain boundary. This is most apparent in Fig. 14(f), where the tool length clearly limits the length of the ‘spikes’ connected to the core part. The introduced design and volume restrictions strongly affect part performance, with Fig. 14(d–f) reaching only 79, 33 and 15% of the performance of case Fig. 14(b).

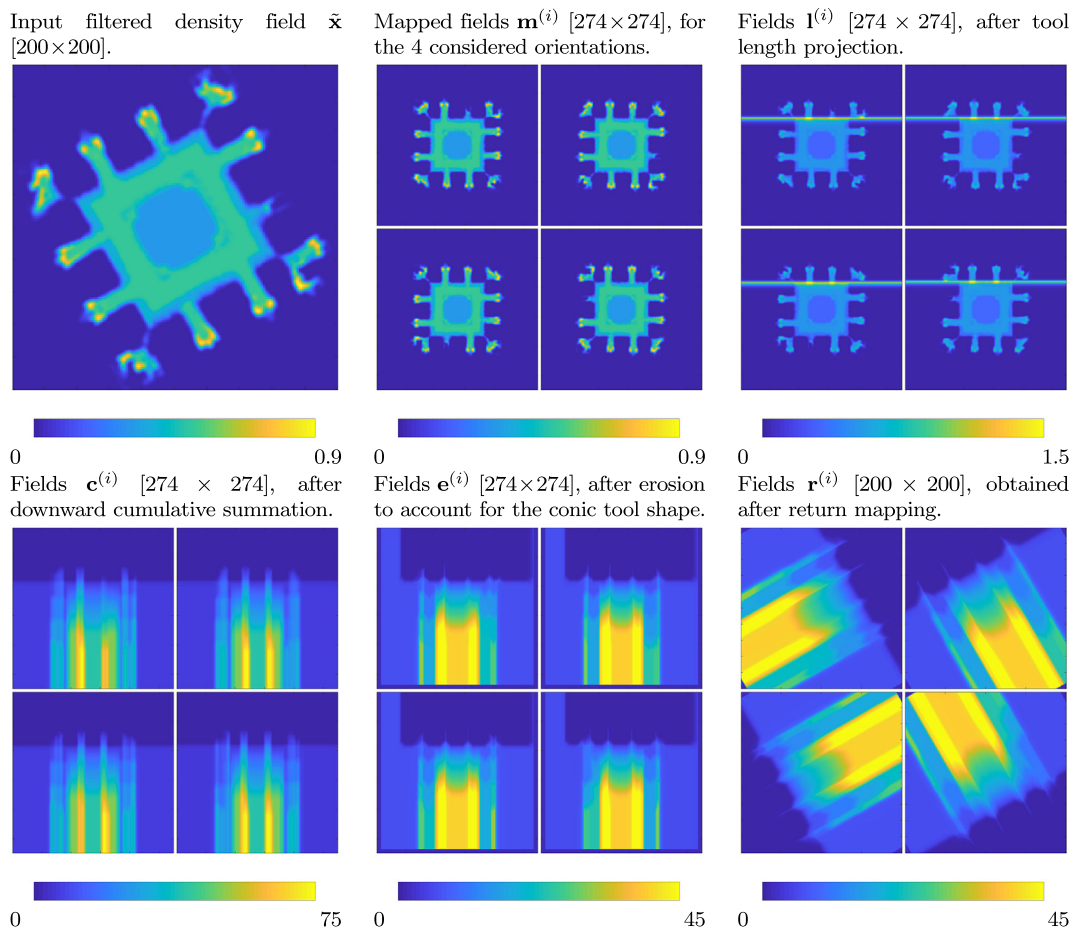


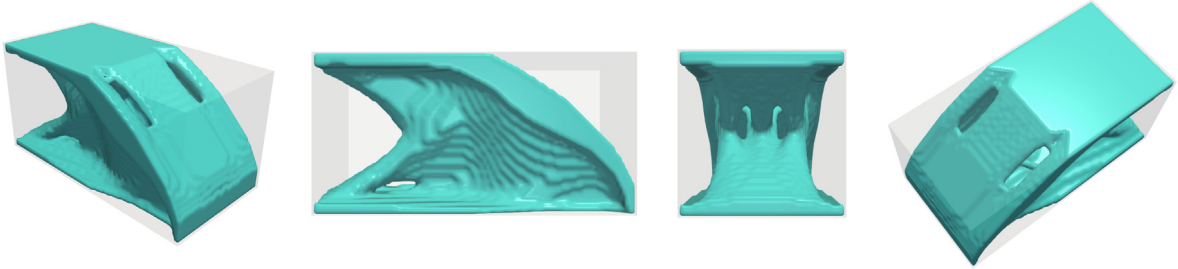
Fig. 15. Intermediate fields of the design shown in Fig. 14(f), where a conic tool was considered of 15 elements in diameter and 25 elements long, in four tool orientations $\{30^\circ, 120^\circ, 210^\circ, 300^\circ\}$.

Intermediate fields corresponding to Fig. 14(f) are depicted in Fig. 15. The input field $\tilde{\mathbf{x}}$ is common to all orientations, but the subsequent fields are orientation-specific (although with the near-symmetric design most appear similar). Next to the multiple orientations, another difference with Fig. 10 is that now the tool length and shape operators are active, which results in additional intermediate fields. Fields $\mathbf{l}^{(i)}$ all contain a horizontal line, created by the tool length operation: this projects the desired end stop at a depth L measured from the outermost structural feature. In this case, a cutting depth (i.e. tool length) of $25h$ is used, which is close to 10% of the edge length of the plotted domain. The line is swept downward in the cumulative summation step (fields $\mathbf{c}^{(i)}$). The conic tool shape is imposed by a structured erosion, resulting in the fields $\mathbf{e}^{(i)}$. The effect of the border expansion as described in Section 2.5 can also be recognized near the edges. Note that the structural boundary, as before, is difficult to distinguish visually due to the extended data range. Finally, fields are reoriented to the original orientation, and after taking the intersection and applying Heaviside projection, the density field shown in Fig. 14(f) is obtained.

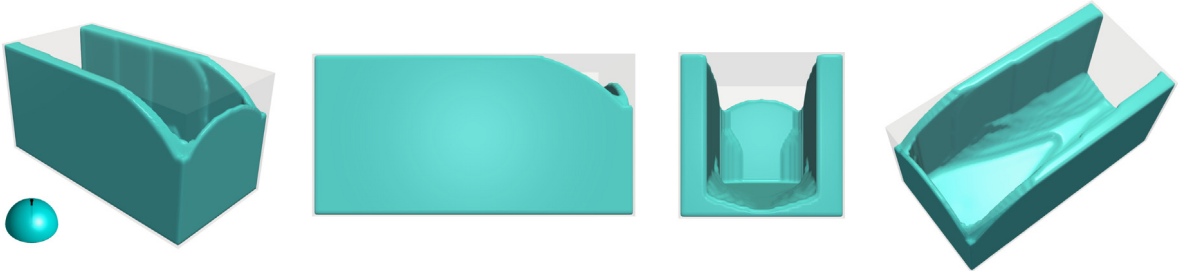
3.3. Machining-based topology optimization tests: 3D

Having confirmed the functionality of the various components of the proposed machining filter in 2D, this subsection focuses on verifying and exploring its effect in a 3D setting. The topology optimization process generates a 3D density field. This has been post-processed by extracting an isosurface at 50% density level, which is subsequently depicted. No other operations (e.g. smoothing) have been applied. Designs are visualized in various views, but to fully convey all geometrical features the corresponding electronic files in U3D format are also provided

a) Reference



b) Machined from top



c) Machined from side

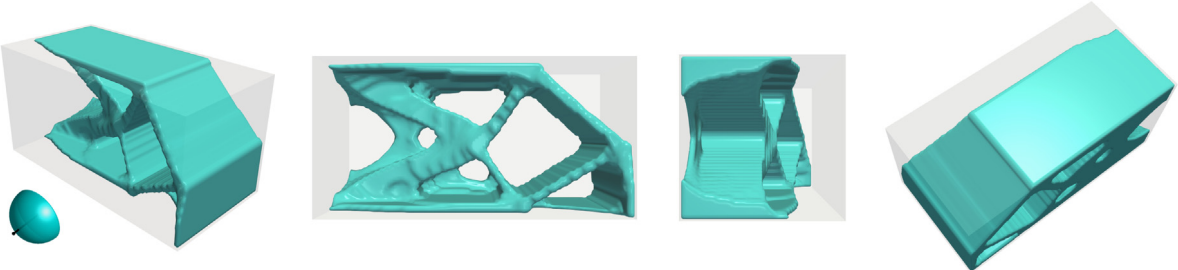


Fig. 16. Cantilever case, reference design (a) and two single-direction machining designs (b,c).

with this manuscript. Note that due to the isosurface extraction process, the volumes of the U3D models will generally not exactly meet the target volume V_{\max} .

3.3.1. Single tool orientation - 2.5D milling

To allow assessment of the individual machining filter components, similar to the 2D study we start by considering a single-direction machining operation. In 3D, this can be seen as a 2.5D milling operation, and also as a casting constraint, treated by several earlier studies (e.g. [3,13]). The proposed formulation reduces to this setting when only a single direction is used. For the mechanical case, we combine this with a flat-tipped cutting tool with a $7h$ diameter (denoted F7). Fig. 16 presents cantilever beam designs obtained in two different single-orientation machining cases (b,c), together with a reference design generated using conventional, unrestricted topology optimization (a). This reference design is not manufacturable through machining, as it contains a hollow chamber in the frontal region with inaccessible surfaces. The 2.5D-machinable cantilevers have very different optimized geometries compared to the reference case, but in terms of compliance the designs are remarkably competitive with only about 5 and 12% higher compliance, respectively, while converging significantly faster. Rounded inside corners can be recognized caused by the applied tool diameter (most apparent in the U3D models). Note also that Fig. 16(c) resembles the 2D reference design, Fig. 8(a).

Results of single-orientation machining optimization for the thermal case are shown in Fig. 17. Here, Fig. 17(a) shows the reference design without machining restriction, featuring a complex and detailed geometrical structure that cannot be realized by machining. Fig. 17(b) shows the result obtained for a single machining direction, with a $5h$ -diameter flat-tipped cutting tool (denoted F5) and no restrictions on tool length. The same case with a stepped

a) Reference

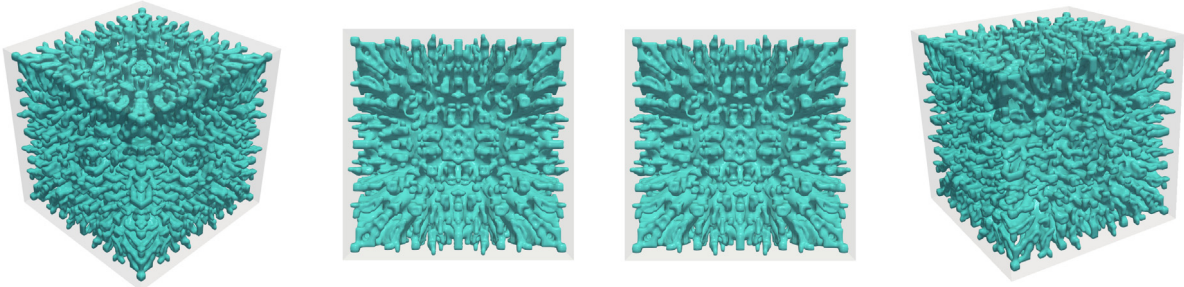
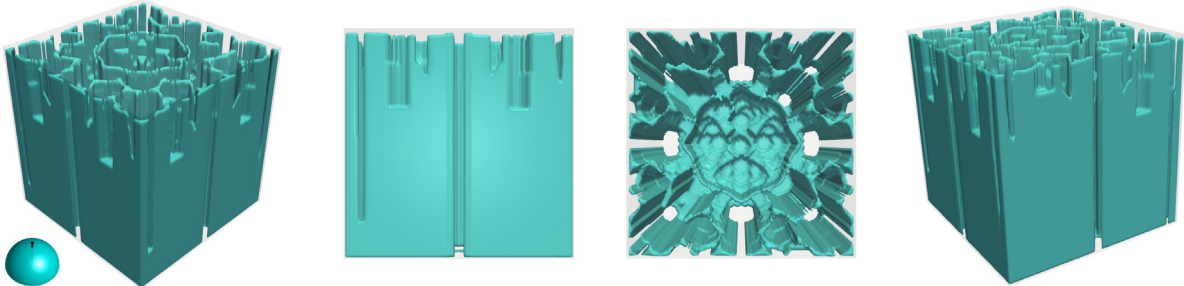
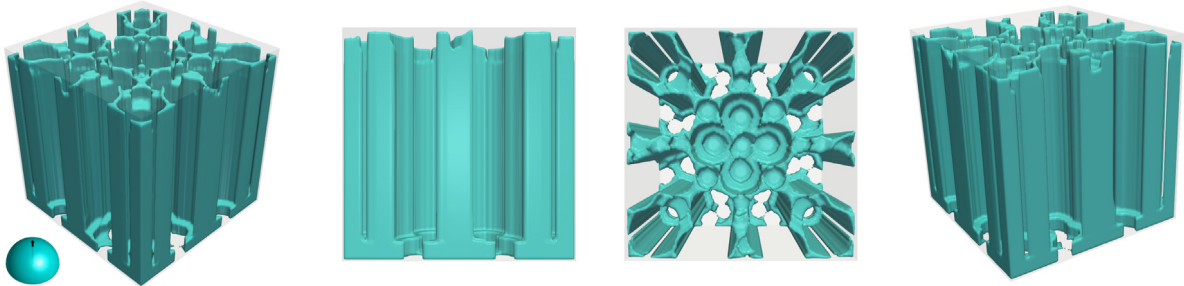
b) Machined from top, with $5h$ -diameter flat-tipped toolc) Machined from top, with $5h$ -diameter/ $9h$ -diameter stepped tool

Fig. 17. Thermal case, reference design (a) and two single-direction machining designs (b,c) with different tool shapes.

tool ($5h$ -diameter flat tip of length $4h$, on a $9h$ -diameter shaft, denoted S5-9) is given in Fig. 17(c), where the imprint of the stepped tool tip can be recognized in the resulting design. The restrictions have a strong impact on performance, case (b) and (c) are a factor 6.4 and $9.4\times$ worse than the reference design. The heat sink is positioned in the center of the cube-shaped design domain, and for good heat conduction material must be present there. With a single machining direction, consequently below the center a solid block of material remains, which leaves less material for other regions. The fact that the heat load is distributed throughout the entire domain makes that any open region has a detrimental effect on the objective, and combined these two aspects result in the observed strong decrease in performance. Hence, for this problem in particular, the 2.5D machining setting comes with a high performance penalty.

3.3.2. Multiple tool orientations — 5-axis machining

Subsequently the set of orientations is extended, to represent a multi-axis milling scenario. While any orientation can be represented in the machining filter, here we consider situations where the part is mounted on a plane, and tools can approach the part axially from directions contained in a hemispherical domain. Three sets of multiple directions are used, depicted in Fig. 18 and defined as follows. The coarsest set consists of 5 orthogonal (unit) directions within the hemisphere, aligned with the domain axes. The middle set has 17 directions, obtained by adding averages of each pair of neighboring directions of the coarse set (8) and each triplet of neighboring directions of the coarse set,

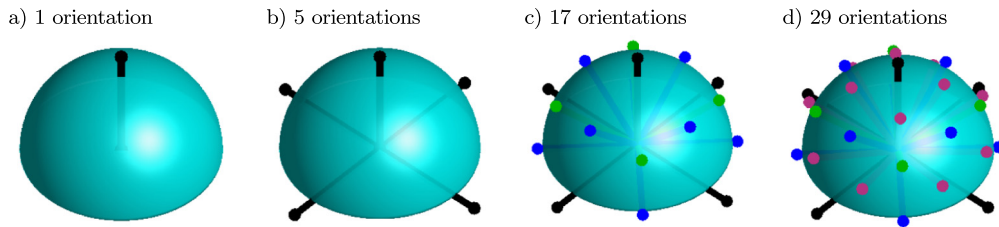


Fig. 18. Machining tool orientation sets considered in this study. For the mathematical definition of these sets, see Table 3.

Table 3

Tool axis directions used in the considered 3D test problems. These unit vectors point in the insertion direction. For readability, $\zeta = 1 + \sqrt{3}$ and $\chi = \sqrt{2 + \zeta^2}$.

Coarse set			Middle set additions			Finest set additions		
x	y	z	x	y	z	x	y	z
1	0	0	$1/\sqrt{2}$	0	$1/\sqrt{2}$	ζ/χ	$-1/\chi$	$1/\chi$
-1	0	0	$-1/\sqrt{2}$	0	$1/\sqrt{2}$	ζ/χ	$-1/\chi$	$-1/\chi$
0	0	1	$-1/\sqrt{2}$	0	$-1/\sqrt{2}$	$-\zeta/\chi$	$-1/\chi$	$1/\chi$
0	0	-1	$-1/\sqrt{2}$	0	$-1/\sqrt{2}$	$-\zeta/\chi$	$-1/\chi$	$-1/\chi$
0	-1	0	$1/\sqrt{2}$	$-1/\sqrt{2}$	0	$1/\chi$	$-1/\chi$	ζ/χ
			$-1/\sqrt{2}$	$-1/\sqrt{2}$	0	$-1/\chi$	$-1/\chi$	ζ/χ
			0	$-1/\sqrt{2}$	$1/\sqrt{2}$	$1/\chi$	$-1/\chi$	$-\zeta/\chi$
			0	$-1/\sqrt{2}$	$-1/\sqrt{2}$	$-1/\chi$	$-1/\chi$	$-\zeta/\chi$
			$1/\sqrt{3}$	$-1/\sqrt{3}$	$1/\sqrt{3}$	$1/\chi$	$-\zeta/\chi$	$-1/\chi$
			$1/\sqrt{3}$	$-1/\sqrt{3}$	$-1/\sqrt{3}$	$1/\chi$	$-\zeta/\chi$	$1/\chi$
			$-1/\sqrt{3}$	$-1/\sqrt{3}$	$-1/\sqrt{3}$	$-1/\chi$	$-\zeta/\chi$	$1/\chi$
			$-1/\sqrt{3}$	$-1/\sqrt{3}$	$1/\sqrt{3}$	$-1/\chi$	$-\zeta/\chi$	$-1/\chi$

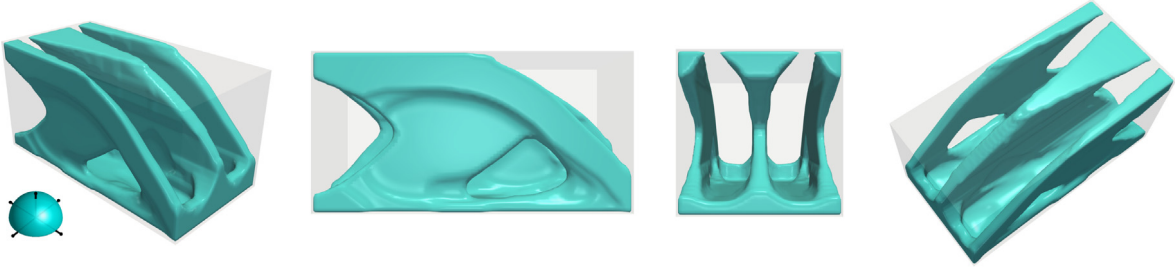
yielding another 4 ‘diagonal’ directions. The finest set considered here has 29 directions in the hemisphere, where 12 directions are added to the middle set by averaging the 4 diagonal directions with each of the three associated orthogonal directions. All vectors contained in the three direction sets are listed in Table 3 at the end of this paper.

Figs. 19 and 20 show cantilever designs obtained for each of these three sets, for the mounting surface taken as the base plane ($y = 0$) and a side plane ($z = 0$), respectively. The machining directions are indicated for each case on a hemisphere in the leftmost figure. Different topologies are seen in Fig. 19(a,b,c), while the designs in Fig. 20 show only subtle differences. The best design is the ‘three-plate concept’ shown in Fig. 19(a), obtained for the coarsest orientation set. Apparently the results of the extended sets (Fig. 19(b,c)) are inferior local optima, as the coarse orientations are included in those sets as well. However, compliances differ less than 4% between all the designs, so the amount of directions in the tool orientation set is not very influential for this problem.

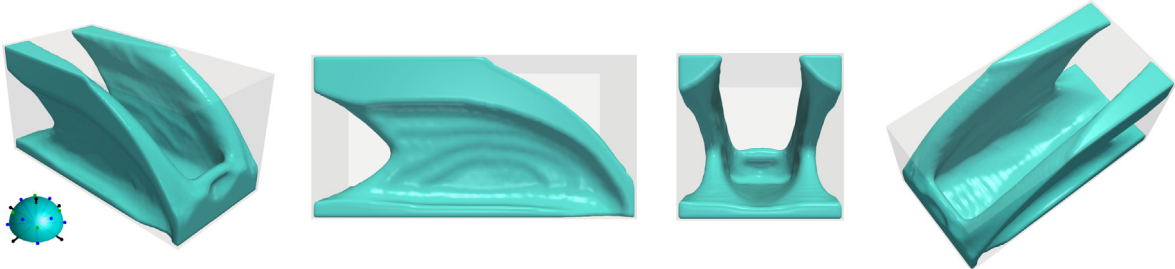
The same tool orientation sets are considered in the thermal case, combined with the flat and stepped tool shapes introduced above. Given the symmetry only a single clamping plane scenario is used. Fig. 21 shows the generated designs for the flat tool (F5), Fig. 22 for the stepped tool (S5–9). The influence of an increased number of directions on the designs is stronger than in the cantilever cases, and also the size of the employed tool clearly affects the obtained design. While a certain degree of symmetry can be observed, similar to the 2D cases it is not perfect and in some cases clearly broken (most apparent in Fig. 22(b)). All cases converged within the allowed 100 iterations, with some in less than 50 (Fig. 21a,c). Compared to the 2.5D-milling case, the performance of the reference design is approached much better by these multi-axis milling designs, with the difference ranging from a factor $1.2\times$ to $1.9\times$. For both tool shapes, the best performance is again obtained with the coarsest direction set, indicating that the other designs are inferior local optima. Potentially the finer sets could benefit from higher aggregation parameters for the intersection operation, P_I (see also Section 3.2.3). However, in general there is no consistent trend between performance and number of directions, and the influence of local minima cannot be excluded.

The final 3D test cases concern the influence of tool length, in addition to tool shape and multiple directions. The middle direction set with 17 orientations is used, with the workpiece clamped at its base. In the mechanical cases, the flat-tipped tool (F7) used also in the preceding examples, is restricted to lengths of $40h$ and $30h$, respectively.

a) 5 orientations



b) 17 orientations



c) 29 orientations

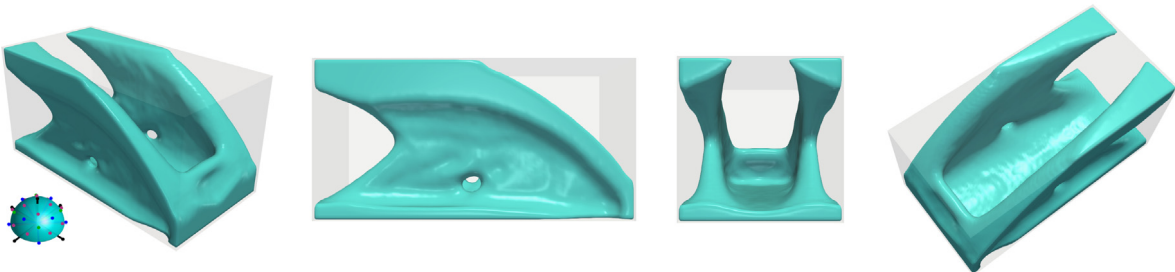


Fig. 19. Mechanical case, for multiple machining tool orientations.

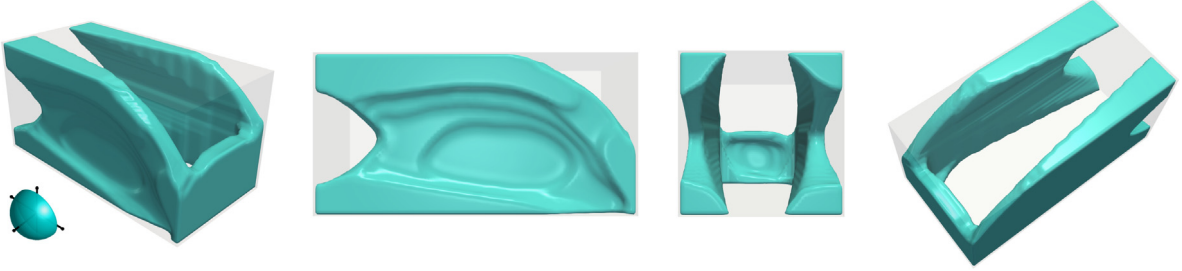
Results are shown in Fig. 23. Clearly the limited tool length forms a more stringent restriction of the design space, although some likeness to the previous cantilever designs is present in the obtained geometries. As the tool is too short to cut to a sufficient depth from the top, access from the side is also needed, which results in design modifications. The difference from the reference design performance increases from 5% to 18 and 22%, for the longer and shorter tool case.

In the thermal case, the stepped tool (S5–9) is used with lengths of $30h$ and $20h$, and results are depicted in Fig. 24. While the topologies are clearly affected, the impact on performance is comparatively small in the $30h$ -case (5% worse than Fig. 22(b)), thus it seems that this tool length is not limiting. The design for the shorter tool, on the other hand, performs 45% worse, and $2.9\times$ worse than the reference. The geometry also no longer extends to the boundaries of the design domain, and the way the tool length is defined relative to the outermost workpiece feature is essential here to correctly represent this manufacturing restriction.

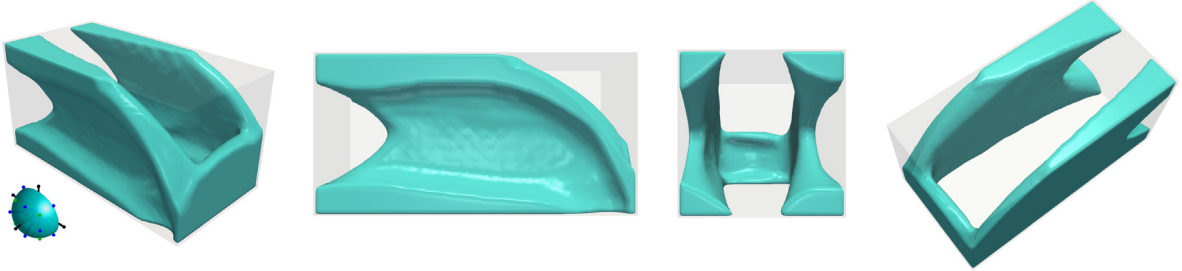
3.4. Application case: GE engine bracket

As a final case, an engine mounting bracket is considered. It is inspired on the full problem definition given in [27] and [29]. In contrast to the original strength-based problem, we treat it as a summed compliance minimization involving four load cases. For the settings used in this study, see Table 1. Four manufacturing scenarios are considered: (a) reference design without restrictions, (b) Machining case with 29 tool orientations, minimal tool diameter ($1h$), (c) Machining with 29 tool orientations, flat tool with diameter $7h$ (F7), and (d) metal additive manufacturing case, considering a critical overhang angle of 45° . In the latter case, we seek a self-supporting design,

a) 5 orientations



b) 17 orientations



c) 29 orientations

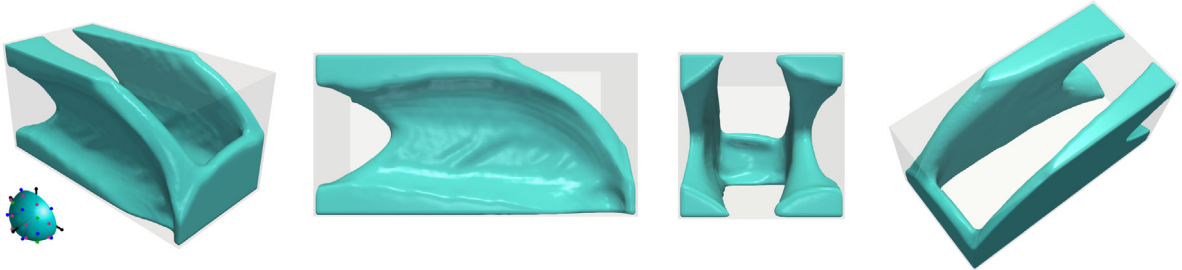


Fig. 20. Mechanical case, for multiple machining tool orientations, clamped on side plane.

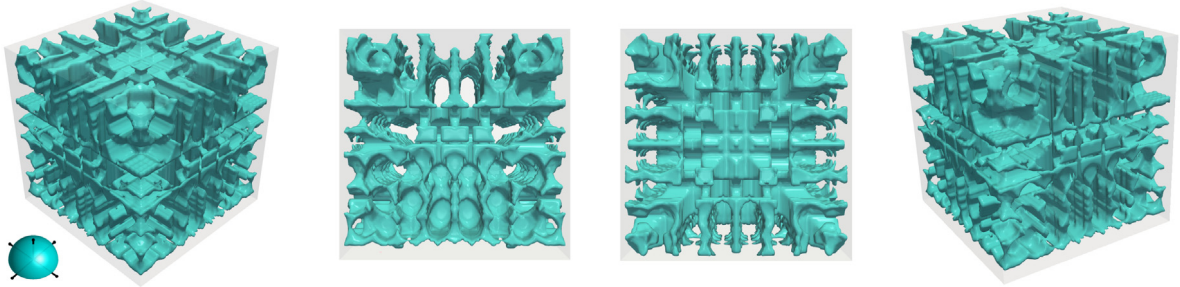
i.e. printable without additional support material. For this, the AM filter proposed in [30] is applied, with its default settings. In all cases, to restrict the designable region of the box-shaped computational to the part envelope shown in Fig. 7(c), non-design regions are enforced by a penalty term added to the objective f , given by:

$$f = \frac{1}{C_{ref}} \sum_{i=1}^4 C_i + \frac{P}{M} \sum_{j=1}^M (\rho_j - \hat{\rho}_j)^2. \quad (22)$$

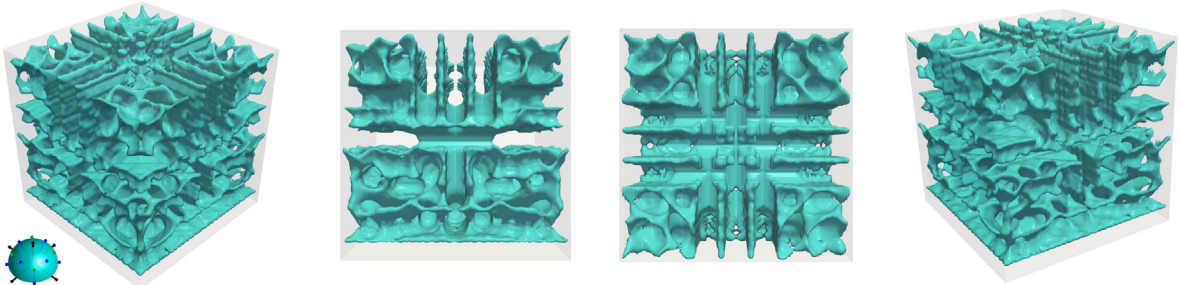
Here C_i is the compliance of load case i , C_{ref} is a suitable normalization factor for the compliance terms, P is a penalty factor (here 5000) to enforce the M individual non-design densities $\hat{\rho}_j$ (0 or 1). Normalization is performed such that the compliance objective term equals 10 in the first iteration. The penalty-based approach is used to impose non-design regions, because these prescribe physical densities ρ , which cannot directly be controlled by fixing the corresponding design variables because of the manufacturing filters involved. A similar approach was introduced in [31] for the AM case.

Fig. 25 shows the designs obtained in all four scenarios. It is observed that the machined design slightly outperforms the reference design, when the finest tool setting is used. Clearly the generated reference design is an inferior local optimum, as nothing prevents the optimization process from producing a similar design as obtained in case (b). In case (c), the larger tool results in a difference of 20% with the reference, and has a smoother appearance (best seen in the U3D file). No post-optimization smoothing was applied, it appears that the aggregation-based erode operation that enforces the tool shape causes this, resulting in a smoother density field. The printed design shows the lowest performance (highest compliance), as it is forced to sacrifice some material to create supporting struts

a) 5 orientations



b) 17 orientations



c) 29 orientations

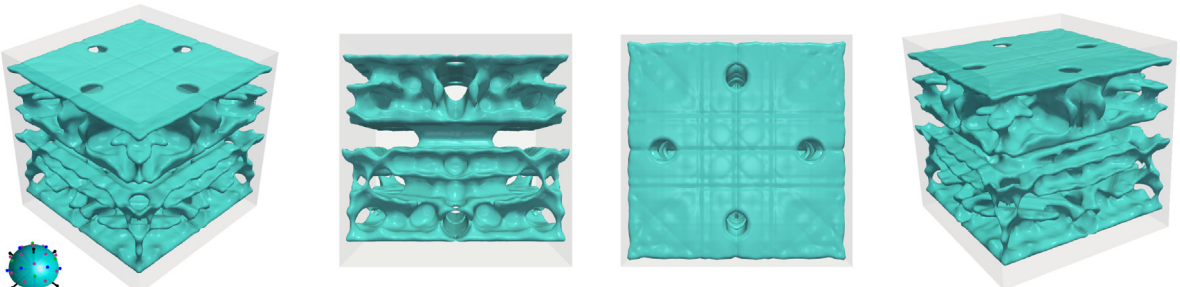


Fig. 21. Thermal case, for multiple machining tool orientations, using a flat-tipped tool of diameter $5h$.

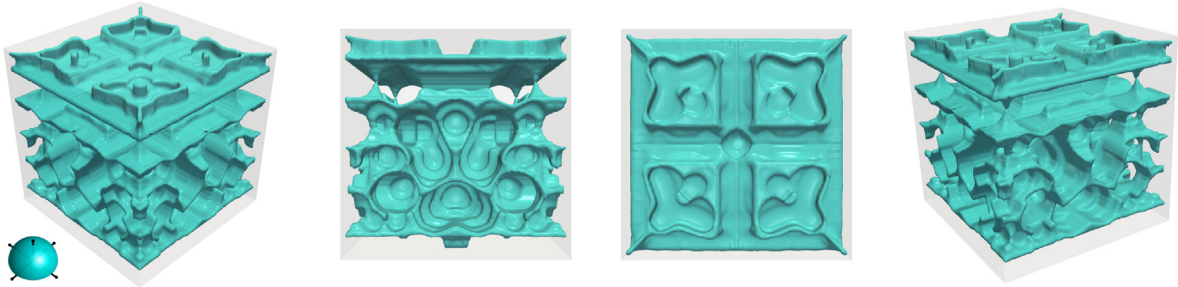
in order to render the upper section printable. Note also that the two upper holes are no longer circular but have a droplet-like shape, caused by the 45° critical overhang angle. Both these holes (void) and the surrounding ring (solid) were defined as non-design regions, note that the penalty formulation allows the optimizer to locally deviate from this when it contradicts the manufacturing conditions.

It is found that the proposed machining filter is capable to enforce multi-axis machining restrictions on realistic cases. It is of interest to also report on the computational cost for this 29-orientation example. For case (c), including tool shape enforcement, 12% of each iteration was spent on average on machining-related operations (including sensitivity analysis), and 0.7% of the total runtime was spent on initializations related to the machining filter (mainly mappings set-up). Note that the four load cases were evaluated in parallel. In case (b), the cost reduces to 4% per iteration. With increasing tool size and number of orientations, these costs will increase proportionally, yet the applied values give a representative indication. The finite element analysis forms by far the main cost component, and the addition of the machining filter only increases the total computational cost by a small fraction.

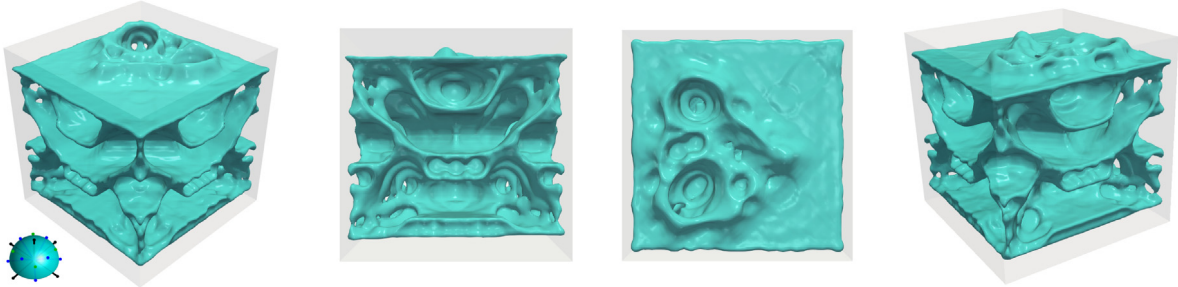
4. Discussion

The preceding numerical examples indicate that the proposed machining filter is effective in imposing multi-axis machining restrictions, at a relatively low computational cost. The presented filter can be adapted in various ways for specific use cases. For example, it is straightforward to define a different tool length or shape for each orientation, when this is desired. Also when the clamping condition of the workpiece is such, that only a subset of all possible

a) 5 orientations



b) 17 orientations



c) 29 orientations

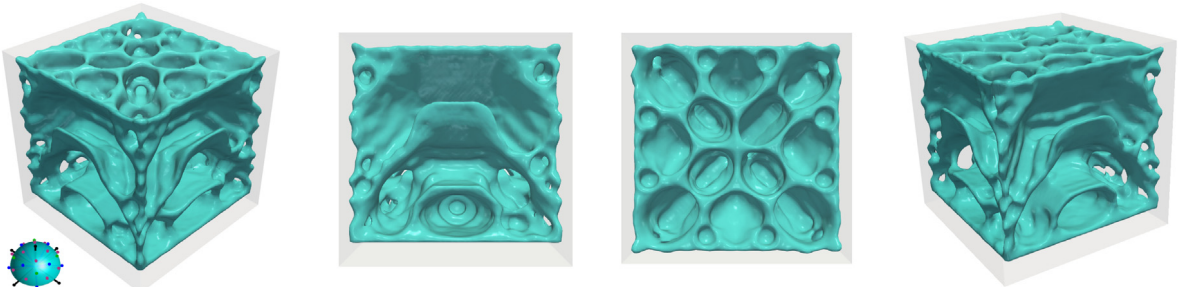


Fig. 22. Thermal case, for multiple machining tool orientations, using a stepped tool of diameters $5h$ and $9h$.

tool insertions can be realized for a given orientation (e.g. insertion parallel to the clamping plane is only possible from a certain distance of this plane), this can be implemented quite easily by defining non-design solid densities in the corresponding part of the mapped density field $\mathbf{m}^{(i)}$.

For the considered 3D problems, no significant performance increase was observed when the set of tool orientations was expanded beyond 5 directions. This is however problem-dependent, and there may be problems where including even more than the 29 orientations used in the finest set is beneficial. All presented results are likely to be local optima, given the nonlinear, non-convex and large-scale nature of the involved optimization problems. In several multi-axis cases, it could be concluded that the gradient-based optimization process was trapped in an inferior local optimum, as increasing the design freedom by additional tool orientations should result in at least equal and potentially better performance.

The manufacturing-related design restrictions were found to sometimes increase the need for penalization of intermediate densities, particularly in the thermal problems with distributed heat input. This can be understood from the perspective that the restrictions force the optimization process to deviate from the unrestricted optimal design, and when this leads to significant worsening of the objective it can become a competitive option to include more intermediate density regions. Similar observations have been made for other manufacturing constraints [3]. Sufficient penalization counteracts this tendency, but at the same time increases non-convexity. Possibly a continuation approach could be helpful in obtaining high-quality local optima, this has not been explored in this study.

The same holds for other problem parameters, such as those of the KS aggregation, the Heaviside projection, and also the initial design. Given the non-convex nature of the problem, results are inevitably parameter-dependent and

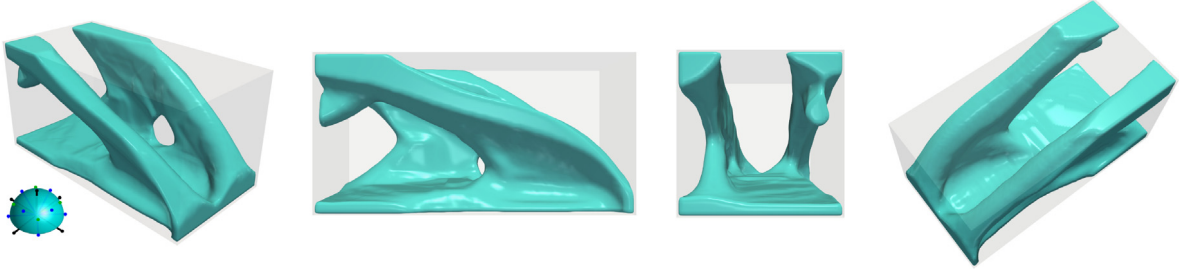
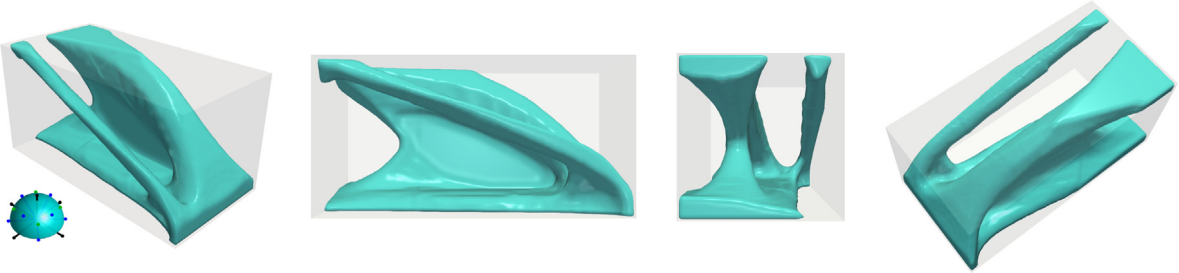
a) Tool length $40h$ b) Tool length $30h$ 

Fig. 23. Mechanical case with 17 orientations and $7h$ -diameter flat-tipped tool, at different tool lengths.

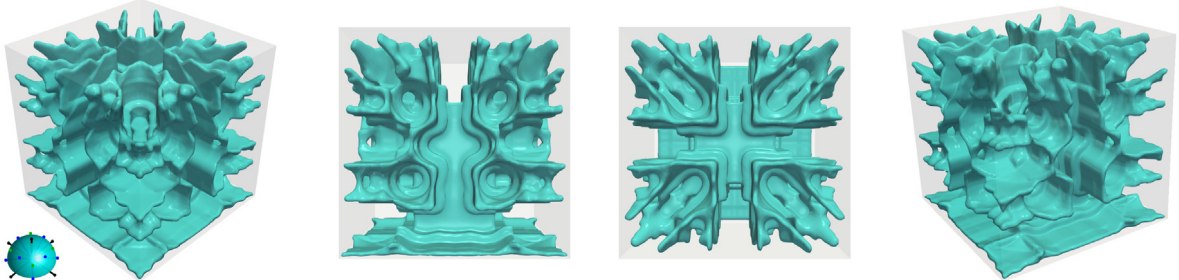
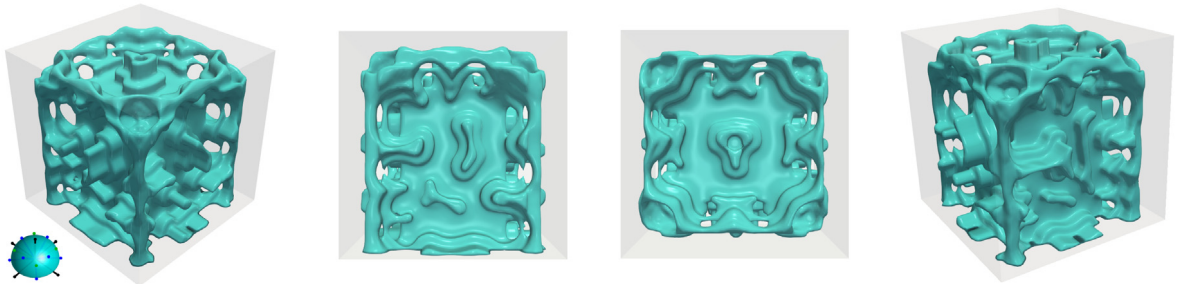
a) Tool length $30h$ b) Tool length $20h$ 

Fig. 24. Thermal case with 17 orientations and $5h$ - $9h$ stepped tool, at different tool lengths.

some experimentation with these parameters may result in performance improvements. The parameters used in this study are based on a limited number of initial trial runs combined with the principle that it is generally beneficial for optimization convergence to limit strong nonlinearities, i.e. excessive parameter increases should be avoided. A full characterization is beyond the scope of this paper and the applied parameter values are almost certainly not optimal. Nevertheless, the fact that the default parameters resulted in adequate designs and decent convergence behavior for a considerable variety of cases indicates that they seem suited for practical use.

- a) No manufacturing considered. $C/C_a = 100\%$. b) Machining, minimal tool size. $C/C_a = 97\%$. c) Machining, tool diameter $7h$. $C/C_a = 121\%$. d) Additive manufacturing from base. $C/C_a = 132\%$.

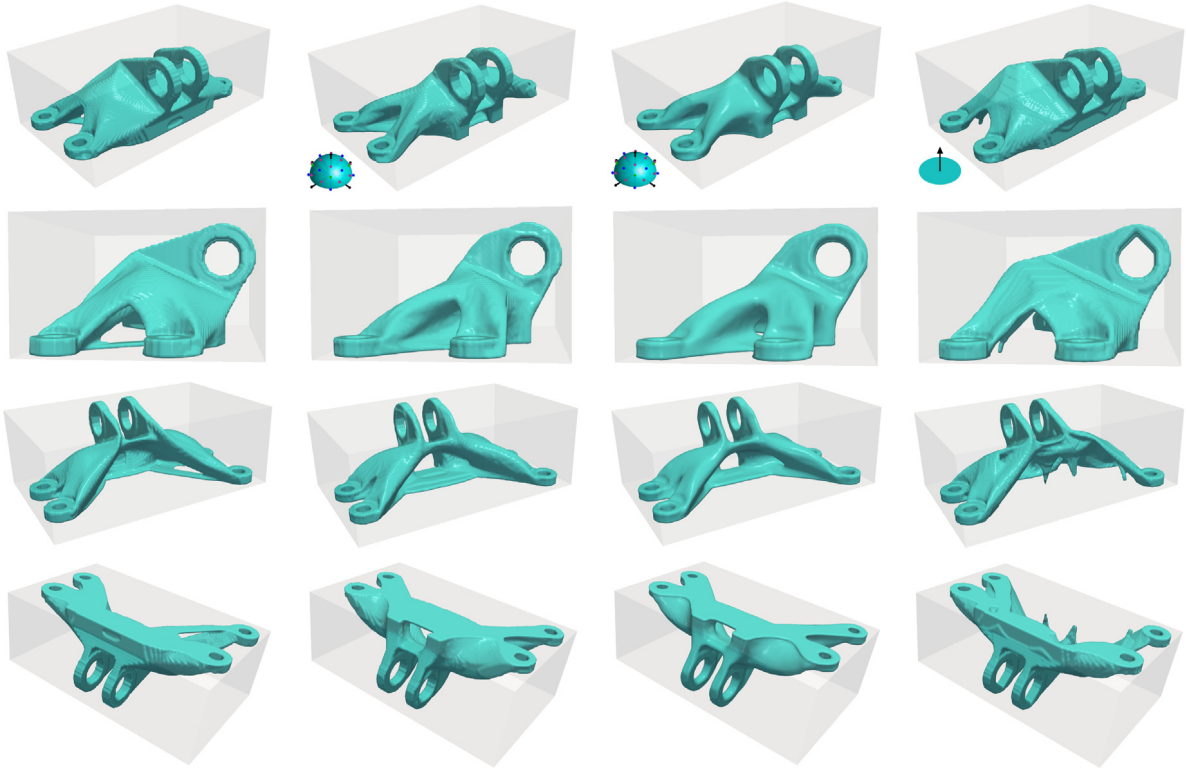


Fig. 25. Optimized designs obtained for the GE engine bracket case, for various manufacturing restrictions.

A limitation of the presented approach is that it is assumed that cutting tools can be axially inserted and retracted. This excludes slot-cutter tools, that are shaped as side-cutting discs connected to a smaller-diameter shaft. These tools can follow a toolpath that enters and exits a workpiece perpendicular to the tool axis, and thus create undercuts that are not possible with the proposed machining filter. The inclusion of such cutting tools is left as a challenge for future research. It probably requires consideration of the actual tool trajectory, a complication that the present formulation avoids.

Another direction for future research is the optimization of the clamping orientation of the workpiece. Separate optimizations can be performed for different orientations, as demonstrated in Figs. 19 and 20, but this is costly when many candidate workpiece orientations must be considered. Perhaps a form of simultaneous optimization of workpiece orientation under machining restrictions is possible, similar to the way this has been demonstrated for part and build orientation optimization for additive manufacturing (AM) [22]. An even more challenging extension is to allow the optimization process to employ a sequence of different clamping orientations.

The final example involved a comparison between multi-axis machining and AM restrictions. In this case, the part optimized for machining outperformed the part optimized for printing, as well as the unrestricted reference design. In general one expects the larger design freedom of AM to translate in superior part performance, but the magnitude of this improvement depends strongly on the specific problem. To make a rational choice between different manufacturing options in terms of cost and performance, it is essential to have optimization methods available that can generate optimized designs for each specific technology. The proposed filter extends the set of manufacturing-oriented topology optimization approaches to include multi-axis machining.

Next to contrasting additive and subtractive processes, there is interesting potential in combining them. The proposed machining filter could for example be used to determine whether support material of a printed part can be removed by an automated subtractive process, as it essentially evaluates accessibility of regions given a certain tool shape and orientation. Similar considerations apply to post-print machining operations, and a way to

include these in the design optimization problem has recently been explored in [31]. Also the trend towards hybrid additive–subtractive processes presents new design challenges and opportunities [6,32].

5. Conclusions

While various new topology optimization approaches tailored to additive manufacturing have been proposed recently, a similar need for dedicated topology optimization methods exists in conventional subtractive manufacturing. To partly address this need, a filter-based procedure to impose multi-axis machining restrictions in a density-based topology optimization setting is proposed and demonstrated in various 2D and 3D examples. The considered cases indicate that including a modest number of discrete tool orientations is sufficient to obtain well-performing, fully machineable designs. The inclusion of tool length and shape is optional, and does add to the overall nonlinearity and computational expense of the filter. However, it is found that computation time remains well below that of the finite element analysis in typical problems, and optimizations using MMA often converge in under 100 iterations.

The machining filter has been demonstrated and validated on mechanical and thermal compliance minimization problems, its application in other types of problems forms a possible extension of this work. Tool length limitations showed a stronger impact on part performance than changes in cutting tool shape or resolution of tool orientation sets. In an application example (GE engine bracket), the part optimized for multi-axis machining outperformed the design obtained under support-free printability for additive manufacturing. In general it is recommended to consider technology-specific optimizations for different manufacturing processes, to make a rational cost/performance trade-off. Considering optimal combinations of various manufacturing options is seen as an optimization challenge for the future.

While the presented machining filter includes tool geometry aspects as well as tool orientations, in its basic form it essentially describes whether a point in the design domain is accessible by a straight tool or beam from outside. This is a general geometric property that also applies to various other problems, e.g. removability of support structures in additive manufacturing, access for inspection etc. It is expected that the presented approach can also be of use in those applications.

Acknowledgment

The author would like to thank Krister Svanberg for providing the Fortran implementation of his Method of Moving Asymptotes, which was used in this work.

Appendix A. Supplementary data

Supplementary material related to this article can be found online at <https://doi.org/10.1016/j.cma.2019.03.037>.

References

- [1] C. Poli, *Design for Manufacturing: A Structured Approach*, vol. 1, Butterworth-Heinemann, 2001.
- [2] M. Bendsøe, O. Sigmund, *Topology Optimization - Theory, Methods and Applications*, Springer-Verlag, Berlin, 2003.
- [3] S.L. Vatanabe, T.N. Lippi, C.R. de Lima, G.H. Paulino, E.C. Silva, Topology optimization with manufacturing constraints: A unified projection-based approach, *Adv. Eng. Softw.* 100 (2016) 97–112.
- [4] J. Davim, *Machining: Fundamentals and Recent Advances*, Springer Science & Business Media, 2008.
- [5] M. Simons, Additive manufacturing – a revolution in progress? Insights from a multiple case study, *Int. J. Adv. Manuf. Technol.* 96 (1–4) (2018) 735–749.
- [6] J. Liu, Y. Ma, A survey of manufacturing oriented topology optimization methods, *Adv. Eng. Softw.* 100 (2016) 161–175.
- [7] A. Sutradhar, J. Park, P. Haghghi, J. Kresslein, D. Detwiler, J.J. Shah, Incorporating manufacturing constraints in topology optimization methods: A survey, in: *ASME 2017 International Design Engineering Technical Conferences and Computers and Information in Engineering Conference*, American Society of Mechanical Engineers, 2017, V001T02A073–V001T02A073.
- [8] B.S. Lazarov, F. Wang, O. Sigmund, Length scale and manufacturability in density-based topology optimization, *Arch. Appl. Mech.* 86 (1–2) (2016) 189–218.
- [9] J. Liu, Y.-S. Ma, 3D level-set topology optimization: a machining feature-based approach, *Struct. Multidiscip. Optim.* 52 (3) (2015) 563–582.
- [10] M. Zhou, R. Fleury, Y.-K. Shyy, H. Thomas, J. Brennan, Progress in topology optimization with manufacturing constraints, in: *9th AIAA/ISSMO Symposium on Multidisciplinary Analysis and Optimization*, 2002, p. 5614.
- [11] Y. Chen, J. Lu, Y. Wei, Topology optimization for manufacturability based on the visibility map, *Comput. Aid. Des. Appl.* 13 (1) (2016) 86–94.

- [12] J. Lu, Y. Chen, Manufacturable mechanical part design with constrained topology optimization, *Proc. Inst. Mech. Eng. B* 226 (10) (2012) 1727–1735.
- [13] A.R. Gersborg, C.S. Andreasen, An explicit parameterization for casting constraints in gradient driven topology optimization, *Struct. Multidiscip. Optim.* 44 (6) (2011) 875–881.
- [14] J.K. Guest, M. Zhu, Casting and milling restrictions in topology optimization via projection-based algorithms, in: *ASME 2012 International Design Engineering Technical Conferences and Computers and Information in Engineering Conference*, American Society of Mechanical Engineers, 2012, pp. 913–920.
- [15] Q. Li, W. Chen, S. Liu, H. Fan, Topology optimization design of cast parts based on virtual temperature method, *Comput. Aided Des.* 94 (2018) 28–40.
- [16] L. Harzheim, G. Graf, A review of optimization of cast parts using topology optimization. II: Topology optimization with manufacturing constraints, *Struct. Multidiscip. Optim.* 31 (5) (2006) 388–399.
- [17] Q. Xia, T. Shi, M.Y. Wang, S. Liu, A level set based method for the optimization of cast part, *Struct. Multidiscip. Optim.* 41 (5) (2010) 735–747.
- [18] G. Allaire, F. Jouve, G. Michailidis, Casting constraints in structural optimization via a level-set method, in: *Proc. of the 10th World Congress on Structural and Multidisciplinary Optimization*, Orlando, Florida, USA, May 19–24, 2013.
- [19] Y. Wang, Z. Kang, Structural shape and topology optimization of cast parts using level set method, *Internat. J. Numer. Methods Engrg.* 111 (13) (2017) 1252–1273.
- [20] T. Kim, S.E. Sarma, Machinability: Geometric reasoning for cutting, *DIMACS Ser. Discrete Math. Theoret. Comput. Sci.* 67 (2005) 245.
- [21] T. Bruns, D. Tortorelli, Topology optimization of non-linear elastic structures and compliant mechanisms, *Comput. Methods Appl. Mech. Engrg.* 190 (26) (2001) 3443–3459.
- [22] M. Langelaar, Combined optimization of part topology, support structure layout and build orientation for additive manufacturing, *Struct. Multidiscip. Optim.* 57 (5) (2018) 1985–2004..
- [23] G. Kreisselmeier, R. Steinhauser, Systematic control design by optimizing a vector performance index, *IFAC Proc. Vol.* 12 (7) (1979) 113–117.
- [24] O. Sigmund, Morphology-based black and white filters for topology optimization, *Struct. Multidiscip. Optim.* 33 (4–5) (2007) 401–424.
- [25] F. Wang, B. Lazarov, O. Sigmund, On projection methods, convergence and robust formulations in topology optimization, *Struct. Multidiscip. Optim.* 43 (6) (2011) 767–784.
- [26] S. Yan, F. Wang, O. Sigmund, On the non-optimality of tree structures for heat conduction, *Int. J. Heat Mass Transfer* 122 (2018) 660–680.
- [27] W.T. Carter, D.J. Ermo, D.H. Abbott, C.E. Bruck, G.H. Wilson, J.B. Wolfe, D.M. Finkhousen, A. Tepper, R.G. Stevens, The GE aircraft engine bracket challenge: an experiment in crowdsourcing for mechanical design concepts, in: *25th Solid Freeform Fabrication Symposium*, SFF 2014, 2014, pp. 1402–1411.
- [28] K. Svanberg, The method of moving asymptotes - a new method for structural optimization, *Internat. J. Numer. Methods Engrg.* 24 (2) (1987) 359–373.
- [29] GE jet engine bracket challenge, 2018, <https://grabcad.com/challenges/ge-jet-engine-bracket-challenge>, (Accessed 20 June 2018).
- [30] M. Langelaar, Topology optimization of 3D self-supporting structures for additive manufacturing, *Addit. Manuf.* 12 (2016) 60–70.
- [31] M. Langelaar, Integrated component-support topology optimization for additive manufacturing with post-machining, *Rapid Prototyping J.* 25 (2) (2018) 255–265.
- [32] J.M. Flynn, A. Shokrani, S.T. Newman, V. Dhokia, Hybrid additive and subtractive machine tools—Research and industrial developments, *Int. J. Mach. Tools Manuf.* 101 (2016) 79–101.